Graduate School of Natural Sciences

Intrinsic alignments of galaxies with multiple shape measurements and its implications

Master Thesis

Sjoerd Weide, BSc.

Theoretical Physics

Supervisors:

Dr. Christos Georgiou
Utrecht University

Dr. Elisa Chisari
Utrecht University

Second Examiner:

Dr. Tanja Hinderer
Utrecht University

July 2023

Abstract

Cosmology asks questions about the large scale properties of the universe, e.g.: "What is the universe made of?", and "How are things distributed throughout the universe?". To help answer these questions we look at Intrinsic Alignment (IA), the correlation between galaxy shapes and nearby large-scale structures during galaxy formation, alongside gravitational lensing. IA is dependent on the method of shape measurement, since different measurement methods are sensitive to different parts of galaxies, which align differently. In this thesis we investigate the use of multiple shape measurements per galaxy to enhance cosmological constraints.

In Part I, Intrinsic Alignment Amplitude (A_{IA}) and difference in A_{IA} between methods (ΔA_{IA}) are measured using data from the Galaxy And Mass Assembly (GAMA) survey (for redshifts) and the Kilo-Degree Survey (KiDS) (for shapes). Galaxy shapes are determined using the moments-based DEIMOS method. This method includes a weight function, which is varied so that a set of measurements is taken that is sensitive to the outer regions of galaxies, a set that is sensitive to the inner regions of galaxies, and one in between. A random catalog is employed to mitigate large-scale structure effects. Two subsamples, "Reddest" and "Brightest," are selected based on colour and brightness. Common estimators are used to measure galaxy position-galaxy position and galaxy position-galaxy shape correlations, with a modification for galaxy position-difference in galaxy shape correlation. This difference is between the shape measured at the outer regions and the inner regions of galaxies. ΔA_{IA} values of 0.55 ± 0.40 (Brightest) and 0.86 ± 0.74 (Reddest) are obtained, providing upper bounds and indicating potential underlying effects.

In Part II, the impact of multiple shape measurements is forecasted for the Large Synoptic Survey Telescope (LSST). Five tomographic redshift bins and two shape measurement methods per galaxy are considered, resulting in 55 angular shape-shape power spectra. The covariance matrix, accounting for correlated noise, is modeled. Fisher forecasting is employed to predict the covariance matrix of cosmological parameters and assess uncertainties related to the parameter S_8. Reductions in S_8 uncertainty up to 35% (ideal scenario), 20% ('Brightest" like scenario), and 15% ("Reddest" like scenario) are forecasted.

In conclusion, this study demonstrates that utilizing multiple shape measurements per galaxy can enhance cosmological constraints without requiring additional telescope time.

Contents

1 Introduction

Cosmology is 'the scientific study of the large scale properties of the universe as a whole'[1]. It thus aims to answer questions such as "What is the history of the universe?", "What is the shape of the universe and why?" and "What is the universe made out of?". The standard model of cosmology that answers some of these questions is the ΛCDM model. This model states that the universe is (mostly) flat, dominated by dark matter of unknown origin and a cosmological constant, started with a big bang and initial perturbations (that grew into current large structures) generated by a very early inflationary period[2]. This does not answer all questions, since our current models for particle physics do not explain what dark matter or the cosmological constant are, and does not provide us with an adequate source of energy that could have driven inflation.

1.1 Lensing

To learn more about the universe and its properties, many different types of probes have been investigated, one of which is weak gravitational lensing. Gravitational lensing is a consequence of the larger General Relativity theory of gravity, which, among other things, states that the presence of energy (so also matter) bends space-time. When light travels through this bent space-time, it gets deflected from a straight path, and thus gets 'lensed'. When there is a lot of matter, this can cause multiple images of the same source to appear on the night sky, which is called strong lensing. However, lesser amounts of matter will still bend the path of the photons of the source, without creating multiple images. This is called weak lensing and an example can be seen in Figure 1. Weak lensing allows for measurements of the dark matter distribution and is also influenced by the geometry and history of the geometry of space-time[2][3][4][5]. One of the ways weak lensing is measured is by looking at the shape of galaxies. Because the light emitted from different parts of galaxies travel through slightly different regions of space to reach us, they are lensed slightly differently and the apparent shape is thus shifted from the actual shape. This effect is sometimes called gravitational shear or weak lensing shear. This change in shape will be similar for galaxies that are close to each other since their light passes through the same space. Since we do not know the actual shape of galaxies, however, one could assume that galaxy shapes are random. This means the gravitational field in between us and source galaxies can be probed by looking at correlations between galaxy shapes, which would be caused by lensing[2].

1.2 Intrinsic Alignment

However, galaxy shapes are not inherently random. Even without lensing, there is a correlation between the shapes of some galaxies that are close to each other, because they aligned with larger-scale structures when they were formed. This phenomenon, called Intrinsic Alignment (IA), is most prevalent in elliptical, red, pressure-supported galaxies. Because IA may cause similar signals to weak lensing, assuming the wrong IA model or no model at all might influence measured values for cosmological parameters[3]. Thus, furthering the understanding of IA will allow for better compensation when analysing weak lensing statistics. Furthermore, since IA itself depends on the distribution of matter, it can also be used to gain information[6], and not just as an effect that needs to be compensated.

Previous research has shown that the magnitude of IA in a sample, quantified by the intrinsic alignment parameter A_{IA}, depends on the techniques used to measure galaxy shapes[7][8][6] (although this might not always be the case[9]). This can be well understood conceptually using an example outlined in Kirk et al.[3]: Consider a hypothetical scenario where galaxies consist of a central bulge and an outer disk. If the outer disk were to be more strongly aligned than the central bulge, then a method sensitive to the central bulge will have different alignment results than one sensitive to the outer disk.

This is not a realistic picture, as the interaction between different parts of the galaxy may cause their alignments to be related. However, Figure 2 illustrates that the chosen algorithm for determining shapes does influence results. Interestingly, these different results will not be unrelated to each other. Since different parts of a given galaxy will influence each other and since the shapes of different parts of a galaxy are influenced by similar outside forces, the different shapes will be correlated on a galaxy-by-galaxy basis. This means that it is interesting to use multiple shape estimators per galaxy, since the shape noise inherent to these measurements might be partially cancelled by comparing multiple shapes that have correlated noise terms.

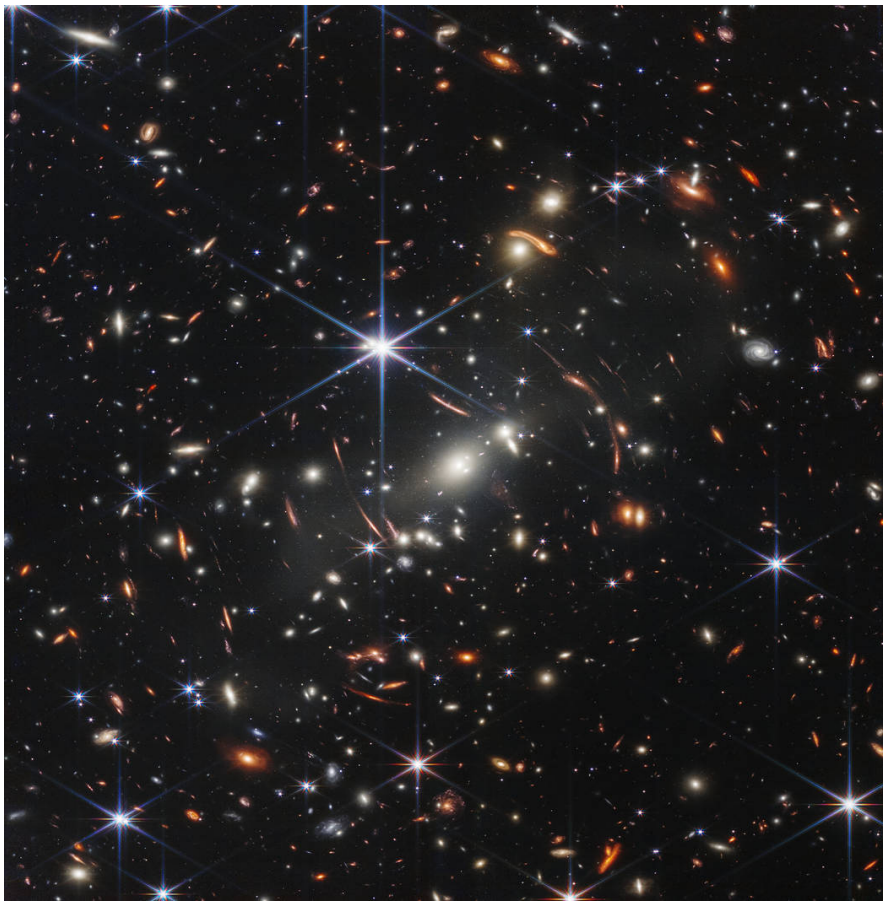

Figure 1: Galaxy cluster SMACS 0723-73 as pictured by the James Webb telescope. It shows a clear example of galaxy lensing as the light from the galaxies around the center is bent so that the galaxies seem to curve around the galaxy cluster in the middle. Image credit: NASA, ESA, CSA, STScI[**JWST˙lensing**].

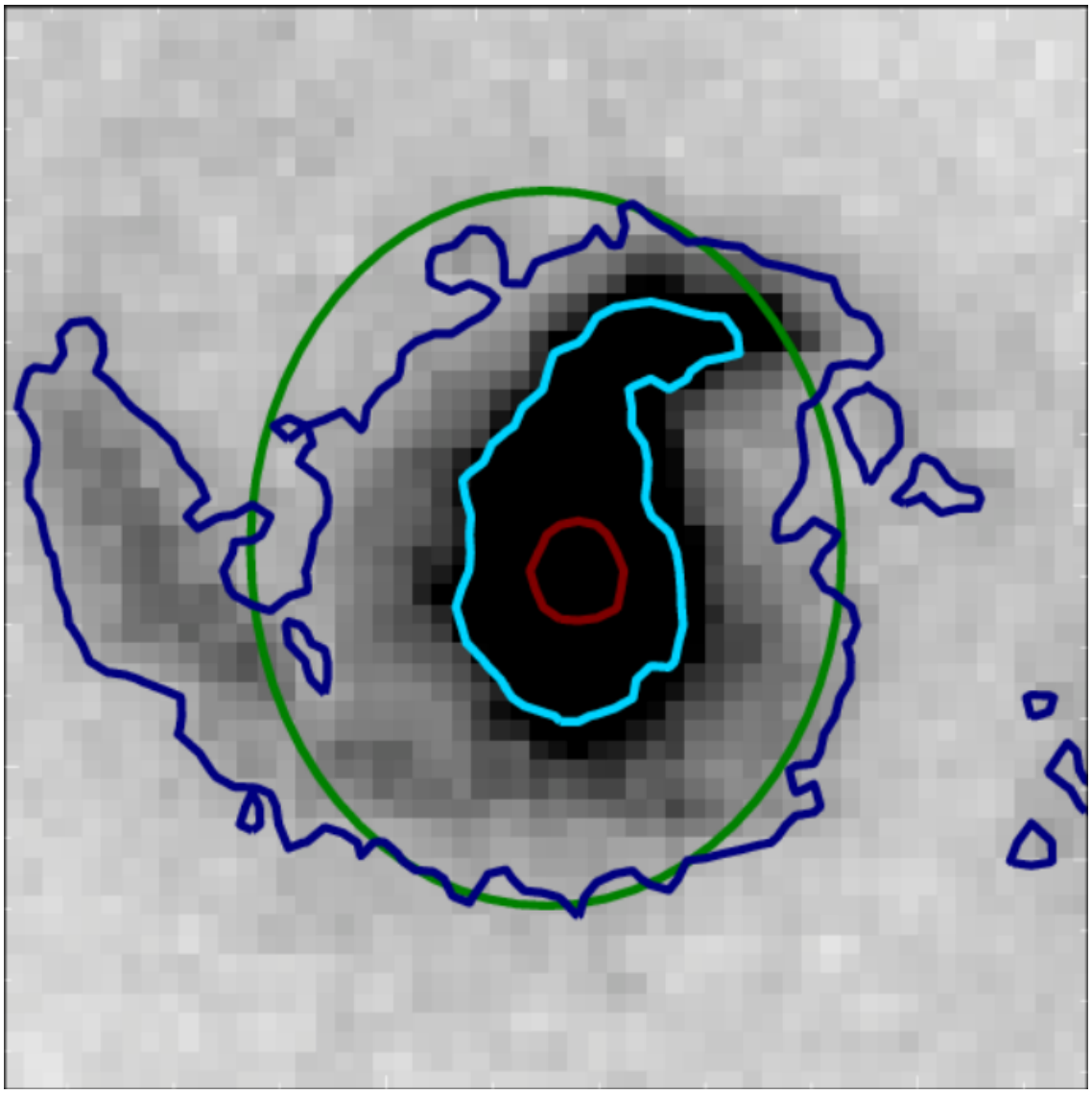

Figure 2: A galaxy observed as part of the COSMOS survey. The dark blue, light blue and red contours are isophotes at 5%, 20% and 50% of the brightest part observed respectively. The green outline is one way to fit an ellipse to this galaxy. The different parts of the galaxy clearly have different shapes and the measured shape will thus depend on how you define galaxy shapes. Image from Kirk et al. (2015)[3].

To probe multiple regions of galaxies, the survey measuring them needs to have a high resolution. The Kilo-Degree survey (KiDS) thus lends itself to multiple shapes analysis, but the upcoming Rubin Observatory's Legacy Survey of Space and Time (LSST) will as well, and covers a larger area of the sky (1500 square degrees versus 20000)[10][11].
In this thesis we will first give a brief general overview of Cosmology and weak lensing, moving on to the matter power spectrum, shape power spectra and why having multiple shapes might be useful in section 2.
In part I, we then focus on the question of whether we are able to measure a difference in alignment signal between different shape measurements. Starting off with an explanation of the data that was used and how it was narrowed down in section 3. Then moving onto how the proper information was extracted in section 4. Finally showing the results in section 5.
In part II, we explore how much the extra information gained from having multiple shape measurements might help constrain cosmological parameters in the upcoming LSST survey. We explain how this forecasting works and what data we used in section 6 and show our results in section 7.
We conclude and wrap up this thesis in section III, ending with an outlook at possible future work.

2 Theory

Since Einstein has described General Relativity (GR), advances in cosmology have provided a clear view of the history of the universe. Starting with the Einstein field equations, which describe how energy influences the curvature of space-time[12][2]:

$$G_{\mu\nu} + \Lambda g_{\mu\nu} = 8\pi G T_{\mu\nu}. \tag{2.1}$$

In this equation, the Einstein tensor ($G_{\mu\nu}$) describes the curvature of space-time, the metric ($g_{\mu\nu}$) describes space-time itself, G is Newton's gravitational constant, the energy-momentum tensor ($T_{\mu\nu}$) describes the energy in the universe and Λ is a constant source of energy of unknown origin. If one now assumes that universe is spatially homogeneous and isotropic, so the same everywhere and the same in all directions, the metric tensor gets heavily restricted. By looking at the 00-component of equation 2.1, modelling the energy-momentum tensor after a perfect fluid and choosing this restricted metric, one discovers one of the Friedman equations[13][2]:

$$\frac{H^2}{H_0^2} = \Omega_{0,r} a^{-4} + \Omega_{0,m} a^{-3} + \Omega_{0,k} a^{-2} + \Omega_\Lambda. \tag{2.2}$$

Here a is the expansion of the universe (normalised at $a = 1$ today), $H^2 = \dot{a}^2/a^2$ characterises the expansion rate of the universe and $\Omega_{r,m,k,\Lambda}$ are the average energy densities of respectively radiation (plus other relativistic particles), matter, curvature of the universe and dark energy, with 0 denoting the value today. The Hubble constant H_0 is often written as $H_0 = 100h\text{kms}^{-1}\text{Mpc}^{-1}$, where h is a dimensionless parameter. This explains the general makeup of our universe, but only at very large scales, where the universe is actually spatially homogeneous and isotropic. Furthermore, the observed values of many components of this equation are in slight contention with values observed in other measurements (for example $H_0 = 69.32 \pm 0.80$km/sec/Mpc, $\Omega_m = 0.2865 \pm 0.0097$ and $\sigma_8 = 0.820 \pm 0.014$ from the cosmic microwave background[14], versus $H_0 = 73.0 \pm 1.4$km/sec/Mpc from Cepheids[15] and $\Omega_m = 0.352^{+0.032}_{-0.031}$, $\sigma_8 = 0.730 \pm 0.054$ from galaxy shapes[16]). Besides that, observations suggest the amount of matter in our universe can not be described by known matter alone, but that about 84 percent of all matter is of unknown origin and about 68 percent of all energy is of unknown origin besides that[17] (we call this unknown energy dark energy). Lastly, this equation only includes the averages of quantities and does not describe how, for example, the matter is distributed on smaller scales.
For more details we look instead at the ΛCDM model. This standard model of cosmology aims to combine observations such as the presence and structure of the cosmic microwave background, the accelerating expansion of our universe and the presence of large scale structures. The resulting picture can be seen in Figure 3. In this model, the universe starts with a big bang, after which the small universe is filled with very hot plasma with quantum fluctuations in its density. The universe then undergoes a brief period of inflation, in which the quantum fluctuations get spread out over the now much larger space. The universe then cools down enough for atoms to form and light to pass in between those atoms, which is how the cosmic microwave

background gets emitted. These atoms then clump together to form stars, seeded by the quantum fluctuations from before inflation. These stars evolve, clump together, die, et cetera. Meanwhile, the universe still expands, being mainly driven by the energy density of matter, which mostly consists of Cold Dark Matter (CDM) of unknown origin. We now enter our current era, where stars have formed galaxies and planets. Now, the expansion of our universe is starting to be driven by dark energy; in our model this dark energy is a Cosmological Constant (Λ).

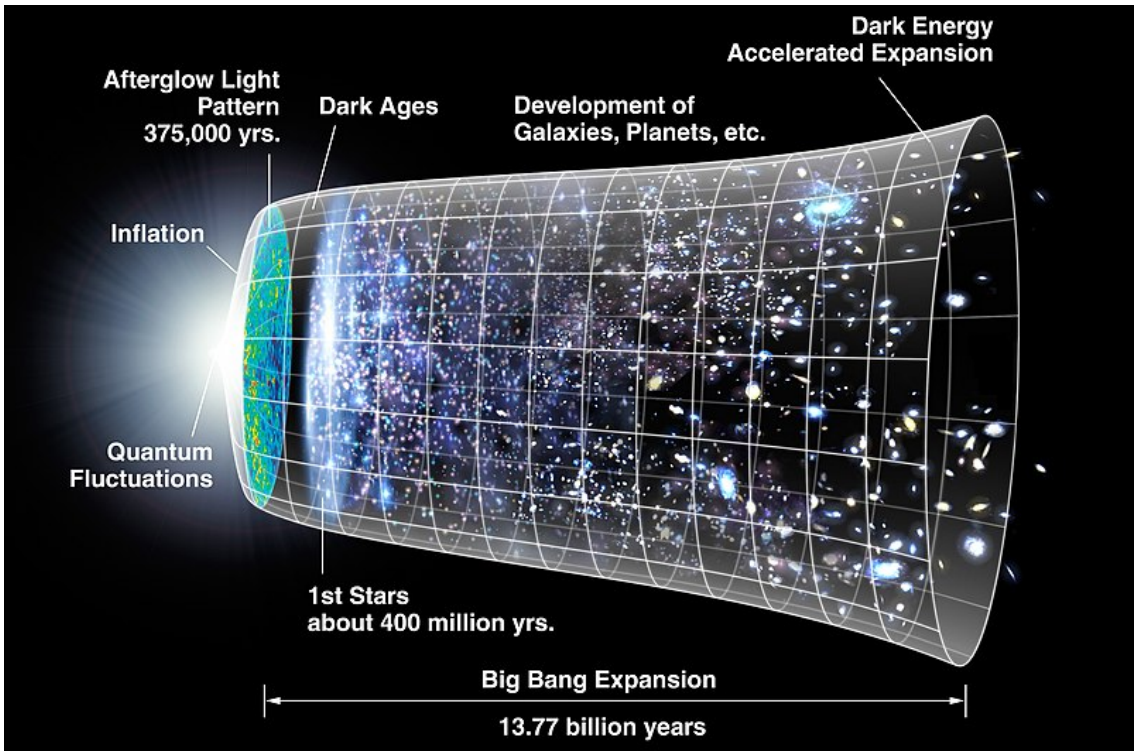

Figure 3: By NASA/WMAP Science Team - Original version: NASA; modified by Cherkash, Public Domain, https://commons.wikimedia.org/w/index.php?curid=11885244

2.1 Matter power spectrum

The following section mostly follows Dodelson's book[2]. To understand the matter distribution in our universe, a useful tool is the matter-matter power spectrum. It describes the distribution of early quantum fluctuations of the matter density in terms of wave numbers. The primordial matter power spectrum, the power spectrum just after inflation, is given by looking at the correlation function of the Fourier transform of the primordial gravitational potential ($\tilde{\phi}_p(k)$):

$$\left\langle \tilde{\phi}_p(\boldsymbol{k})\tilde{\phi}_p^*(\boldsymbol{k}')\right\rangle \equiv (2\pi)^2 P_{\phi_P\phi_P}(k)\delta_D^3(\boldsymbol{k}-\boldsymbol{k}'). \tag{2.3}$$

Where δ_D^3 is the three dimensional delta function and $P_{\phi_P\phi_P}(k)$ is the primordial density fluctuation power spectrum, which can be predicted from theories of inflation. To get the current power spectrum of matter density fluctuations instead, we relate $\tilde{\phi}_p(\boldsymbol{k})$ to $\tilde{\delta}(\boldsymbol{k},a)$, the Fourier transform of matter density fluctuations. The density fluctuations are defined through

$$\frac{\rho(\boldsymbol{k},a)-\bar{\rho}(a)}{\bar{\rho}(a)} = \delta(\boldsymbol{x},a) = \int e^{i\boldsymbol{k}\cdot\boldsymbol{x}}\tilde{\delta}(\boldsymbol{k},a)d\boldsymbol{k} \tag{2.4}$$

with $\rho(\boldsymbol{k},a)$ the density at a certain scale and scale factor and $\bar{\rho}(a)$ the average density at that scale factor. This is related to $\tilde{\phi}_p(\boldsymbol{k})$ as

$$\tilde{\delta}(\boldsymbol{k}, a) = \frac{3}{5}\frac{k^2}{\Omega_m H_0^2}\tilde{\phi}_p(\boldsymbol{k}')T(k)D_1(a). \tag{2.5}$$

Where $T(k)$ is the transfer function, which tracks the mode-dependent part of the evolution of the potential and $D_1(a)$ is the growth function, which describes scale-independent growth. Together these functions parameterise the growth of the potential. We then look at the matter power spectrum $P_{\delta\delta}(k, a)$, defined through[4]:

$$\left\langle \tilde{\delta}(\boldsymbol{k})\tilde{\delta}^*(\boldsymbol{k}') \right\rangle \equiv (2\pi)^2 P_{\delta\delta}(k)\delta^3(\boldsymbol{k} - \boldsymbol{k}'). \tag{2.6}$$

The expression for the matter power spectrum then becomes using equation 2.5:

$$P_{\delta\delta}(k, a) = 2\pi^2\delta_H \frac{k^{n_s}}{H_0^{n_s+3}}T^2(k)\left(\frac{D_1(a)}{D_1(a=1)}\right)^2 \tag{2.7}$$

With n_s the spectral density index, which is dependent on the inflationary theory and δ_H a normalisation constant. To get to this equation, dark matter was assumed to be cold dark matter, neutrinos were ignored and anisotropic stress was assumed to be absent. Furthermore, the perturbations of the matter field were assumed to be of linear order and higher order perturbations, which are relevant at small scales/high k, were dismissed. This means that the code that solves this equation numerically in practice uses a different approximation at small scales.

2.2 Shape statistics

One of the ways to probe the matter power spectrum experimentally, is by looking at galaxy shapes. Because GR dictates that energy bends the space-time it inhibits, the matter fluctuations described in the matter power spectrum also bend space-time. This means that the light that is emitted by faraway galaxies gets deflected by the bent space-time on its way to us. Since photons emitted from different parts of a galaxy travel trough slightly different regions of space to get to us, they get deflected slightly differently. This results in galaxy shapes, as observed by us, being changed, and allows us to measure the amount of matter causing the bending. A great example of this phenomenon can be seen in figure **??**. As mentioned before, when the lensing effect is less strong, it can still be measured in a statistical fashion. By looking at the correlation of galaxy shapes on a large area of the sky, the power spectrum of the shapes can be measured, which can then be related to the matter power spectrum.
By shape of a galaxy, we mean the ellipse that best approximates the way it get projected on the night sky. This is quantified using the ellipticity (or third flattening)[3]:

$$\begin{pmatrix}\epsilon_1\\ \epsilon_2\end{pmatrix} = \frac{1-q}{1+q}\begin{pmatrix}\cos 2\theta\\ \sin 2\theta\end{pmatrix}. \tag{2.8}$$

Here $q = b/a$ is the axis ratio (semi-minor axis over semi-major axis), θ is the angle of the semi-major axis with some axis of the chosen coordinate system and ϵ_1, ϵ_2 are the ellipticities. If the lensing effect is weak, the true ellipticity of the source $\epsilon^s = \epsilon_1^s + i\epsilon_2^s$ is related to the observed ellipticity through[3]:

$$\epsilon \approx \epsilon^s + \gamma, \tag{2.9}$$

where γ is the complex weak lensing shear. Since weak lensing effects are on average very small, we turn to statistical averages to detect signals instead. The correlation function between two ellipticity components ϵ_i ϵ_j with $i, j \in \{1, 2\}$ is thus[3]

$$\langle \epsilon_i \epsilon_j \rangle = \langle \gamma_i \gamma_j \rangle + \left\langle \epsilon_i^s \epsilon_j^s \right\rangle + \left\langle \gamma_i \epsilon_j^s \right\rangle + \langle \epsilon_i^s \gamma_j \rangle. \tag{2.10}$$

The first term on the right hand side is the cosmic shear self-correlation, often shortened as GG, the second term is the correlation between intrinsic ellipticities, shortened as II, the last two terms are the cross correlation between shear and intrinsic shape, respectively GI and IG, often grouped under GI.
Since the universe is isotropic at large scales, these correlations reduce to zero at large separation of galaxy pairs, at smaller separation, they do not. If intrinsic galaxy shapes were not correlated with each other and thus distributed randomly, the II and GI contributions would disappear and one could measure the cosmic shear auto-correlation by just measuring galaxy shapes. However, when galaxies are formed, they tent to align with the large scale matter distribution. This causes intrinsic galaxy shapes to be correlated and is called Intrinsic Alignment (IA).
This means that the GG term is related to the matter field because of the light from both galaxies travelling through similar space, thus through a similar part of the matter field and thus being lensed in a similar way. The II term is related to the matter field because both galaxies align with the same local matter field. The GI term is related to the matter field by a galaxy closer to us aligning with the same matter field that lenses a galaxy further away from us. This also means that either the GI term of a galaxy pair (with small projected separation, but larger line of sight separation) is expected to be zero, or its IG term is expected to be zero, dependent on which of the two galaxies is closer to us. This can be seen in figure 4.
Thus far we have been talking about ellipticities ϵ_1 and ϵ_2, which depend on the choice of coordinate system, since ϵ_1 represents elongation with respect to a circular galaxy in the x or y direction, and ϵ_2 represents elongation in the directions at an 45° angle with x and y. We can rotate this system to align the x-axis of our choice with the line on the sky connecting two galaxies we are correlating. This means the two components ϵ_+ (tangential) and ϵ_x (cross component) are, respectively, parallel or perpendicular to the line connecting the two galaxies, or at 45° or 135° with respect to the separation line. More formally[3]:

$$\epsilon_+ = -(\epsilon_1 \cos 2\theta + \epsilon_2 \sin 2\theta) = -\mathrm{Re}[\epsilon e^{-2i\theta}] \tag{2.11}$$

and $\epsilon_\times = \mathrm{Im}[\epsilon e^{2i\theta}]$, where θ is the angle between the initial x-axis and the vector from one galaxy to another.

2.3 Intrinsic shape power spectra

To see how this ellipticity relates to the matter power spectrum exactly, we need to look at the correlation function of tangential ellipticity: $\epsilon_+^s = \epsilon^I + \epsilon^{rnd}$

$$\xi_{++}(r_p, \Pi) \equiv \langle \epsilon_+ \epsilon_+ \rangle_{r_p, \Pi} \tag{2.12}$$

where the brackets denote averaging over all galaxy pairs with line of sight seperation Π and projected seperation r_p. Since we will be measuring this on the night sky, it is useful to project this (and other correlations) along the line of sight like[3]:

$$w_{ab}(r_p) = \int W(z) \int \xi_{ab}(r_p, \Pi, z) d\Pi dz \tag{2.13}$$

with

$$W(z) = \frac{p^2(z)}{\chi^2(z)\chi'(z)} \left[\int dz \frac{p^2(z)}{\chi^2(z)\chi'(z)} \right]^{-1} \tag{2.14}$$

being the redshift weighting, $p(z)$ is the galaxy redshift distribution, χ is the comoving distance and a, b are the quantities being correlated.
We can now relate this projected correlation function to the intrinsic-intrinsic power spectrum by using a Hankel transform to express it in terms of Bessel functions[18]:

$$P_{II}(k, z) = 2\pi \int w_{++}(r_p) J_0(k r_p) r_p dr_p, \tag{2.15}$$

where J_n is an n^{th} order Bessel function of the first kind.
We now introduce a model to relate this power spectrum to the matter power spectrum. The linear alignment model assumes linear relation between the ellipticities of galaxies and the gravitational potential quadrupole

at the time of formation of the galaxies. It states that states that fluctuations in the large-scale potential cause perturbations of the ellipticity of the dark matter surrounding galaxies, causing galaxy ellipticities to do so as well. Higher order terms disappear because large-scale fluctuations are small and the intrinsic alignment is thus assumed to be a linear function of the gravitational potential. This leads to the intrinsic-intrinsic power spectrum being related to the matter power spectrum as follows[19][20]:

$$P_{II}(k,z) = \left(A_{IA}C_1\frac{a^2\bar{\rho}(z)}{D(z)}\right)^2 P_{\delta\delta}(k,z). \tag{2.16}$$

Here, $\rho(z)$ is the mean density of the universe, $D(z)$ is the growth factor, encoding the evolution of the matter power spectrum as a function of redshift. C_1 is a proportionality constant that indicates the ratio of the two power spectra and is fixed using simulations to a value of $5 \times 10^{-14} M_{\odot}^{-1} h^{-2} \mathrm{Mpc}^3$. A_{IA} is the Intrinsic Alignment Amplitude, which varies the alignment dependent on galaxy selection and indicates the amount of alignment relative to the calibrated value of C_1. Because A_{IA} depends heavily on, among other things, the redness and brightness of the sample selected, it needs to be restricted on a sample by sample basis.
This model can be improved (as we did) by using the nonlinear matter power spectrum, instead of the linear matter power spectrum[18][21]. This model is called the nonlinear alignment model (NLA) and is a slight improvement upon the linear alignment model. Although the NLA is improved, it can still not successfully probe highly nonlinear scales. Furthermore, it has no physical basis, but fits the data phenomenologically.
When wanting to constrain A_{IA} from this, one notices that there is a degeneracy in its sign, so it is useful to also look at the position-shape and position-position correlation functions given by the NLA[20]:

$$w_{g+}(r_p) = -b_g \int dz W(z) \int_0^{\infty} \frac{dk_{\perp}k_{\perp}}{2\pi} J_2(k_{\perp}r_p) P_{\delta I}, \tag{2.17}$$

$$w_{gg}(r_p) = b_g^2 \int dz W(z) \int_0^{\infty} \frac{dk_{\perp}k_{\perp}}{2\pi} J_0(k_{\perp}r_p) P_{\delta\delta}. \tag{2.18}$$

Here b_g is the linear galaxy bias, which signifies the ratio of the galaxies and the matter overdensities ($\delta_g = b_g\delta_m$) and the shape-position power spectrum is given by[22][20]:

$$P_{\delta I}(k,z) = -A_{IA}C_1\frac{a^2\bar{\rho}(z)}{D(z)} P_{\delta\delta}(k,z). \tag{2.19}$$

So to constrain A_{IA} it is useful to look at w_{g+}, since w_{++} has a degeneracy in the sign of A_{IA} and since the w_{++} signal is generally much weaker.
In practice the alignment of individual galaxies depends on a lot of different factors, such as redness of the galaxy, brightness, whether it is a satellite galaxy or central galaxy, etc. With the ellipticity of a given galaxy given by equation 2.9, it might be useful to group ellipticity effects outside our model under a random contribution[6]. For a given galaxy i:

$$\epsilon_i = \epsilon_i^I + \gamma_i + \epsilon_i^{rnd} \tag{2.20}$$

With ϵ_i^I being the ellipticity as expected by the theory, dependent on the matter field and the shape measurement method, γ_i being the lensing effect and ϵ_i^{rnd} being the random shape noise.
We have so far only looked at $< \epsilon_+\epsilon_+ >$ correlations, but what about $\epsilon_\times$? We expect correlations involving the cross component to disappear at linear order, because there are no forces in those directions at linear order. These correlations can still be used tFsince o test for systematics though, as a significant deviation from zero in these correlations might indicate a problem. We also expect $< \epsilon_\times\epsilon_+ >$ to disappear because of parity between the two.

2.4 Multiple shapes

As explained before, the A_{IA} of a galaxy sample is dependent on the shape measurement method used. As can be seen in Figure 2, an ellipticity measurement with a weighting more sensitive to the outside of the galaxy (like the green ellipse) can get a significantly different value from one that is more sensitive to the

one a bit further in (the light blue region for example). If the ellipticity changed randomly when looking at different scales of the galaxy, could be ignored, since we are looking at averages. However, since the outer region of the galaxy is less gravitationally bound to the galaxy than the inner region, one would expect the outer region to align stronger with the larger matter field. These two hypothetical shape measurements would of course still be highly correlated, since they are measuring the same galaxy. It still might be very useful to have multiple shapes per galaxy however, since it would not cost extra telescope time to measure multiple shapes, but does add information.
To see how differences between different shape measurements would influence statistics, let's start by looking at equation 2.20: The lensing effect is independent of shape measurement method since it only depends on the gravitational potential of the lens and is thus decided by the matter field. The random shape noise will be influenced by similar influences for different measurements of the same galaxy and will thus be strongly correlated.
This means that having multiple shape measurements per galaxy might help improve constraints on cosmological parameters, since one can essentially remeasure the lensing contribution, but with different intrinsic alignment. The expected ellipticity would of course be measurement dependent and thus different, but it would still be correlated amongst shape measurement methods.
To see whether this difference in alignment is actually there and measurable, we take a look at the projected correlation function between the difference in ellipticity and galaxy position. The galaxy position, the lines joining galaxy pairs, the galaxy bias and the redshift weight function should be the same amongst shape measurements of the same galaxy sample. We can find the difference in alignment $\Delta A_{IA} = A_{IA,m} - A_{IA,n}$ between two measurement methods m and n via the difference in ellipticity:

$$\Delta\epsilon_{m,n} = \epsilon^I_m - \epsilon^I_n + \gamma - \gamma + \epsilon^{rnd}_m - \epsilon^{rnd}_n = \Delta\epsilon^I_{m,n} + \Delta\epsilon^{rnd}_{m,n}. \tag{2.21}$$

To find the difference in A_{IA} between the two measurements, one would want to look at w_{g+}, or actually $w_{g\Delta+}$.

$$\Delta\epsilon_+ = -((\epsilon_{1,m} - \epsilon_{1,n})\cos 2\theta + (\epsilon_{2,m} - \epsilon_{2,n})\sin 2\theta) \tag{2.22}$$

$$\xi_{g\Delta+}(r_p, \Pi, z) = \langle g\Delta\epsilon_+ \rangle_{r_p,\Pi} \tag{2.23}$$

$$w_{g\Delta+}(r_p) = \int W(z) \int \xi_{g\Delta+}(r_p, \Pi, z) d\Pi dz \tag{2.24}$$

$$w_{g\Delta+}(r_p) = \Delta A_{IA} b_g \int dz W(z) \int_0^\infty \frac{dk_\perp k_\perp}{2\pi} J_2(k_\perp r_p) C_1 \frac{a^2\bar{\rho}(z)}{D(z)} P_{\delta\delta}(k, z) \tag{2.25}$$

So in our model $w_{g\Delta+}$ only differs from w_{g+} with a constant factor.

2.5 Angular Power spectra

This section mostly follows Section 6.1 in Kirk et al. (2015)[3]. An easy way to combine lensing and intrinsic alignment effects is by using projected angular power spectra in Fourier space. This is a distribution of shape correlation as a function of angular scale on the sky, and given by[3]:

$$C^{(ij)}_{++}(l) = C^{(ij)}_{\mathrm{GG}}(l) + C^{(ij)}_{\mathrm{II}}(l) + C^{(ij)}_{\mathrm{GI}}(l) + C^{(ij)}_{\mathrm{IG}}(l). \tag{2.26}$$

Where i, j are now the different tomographic redshift bins that are being compared. The GI term will be zero if the i bin is significantly further away than the j bin. The contributions of different terms can be seen in figure 4. These power spectra are projected from the 3D power spectra as follows[3]:

$$C^{(ij)}_{\mathrm{GG}}(l) = \int_0^{\chi_H} d\chi \frac{q^i(\chi)q^j(\chi)}{f^2_{\mathrm{K}}(\chi)} P_{\delta\delta}(\frac{l}{f^2_{\mathrm{K}}(\chi)}, \chi) \tag{2.27}$$

$$C^{(ij)}_{\mathrm{II}}(l) = \int_0^{\chi_H} d\chi \frac{p^i(\chi)p^j(\chi)}{f^2_{\mathrm{K}}(\chi)} P_{\mathrm{II}}(\frac{l}{f^2_{\mathrm{K}}(\chi)}, \chi) \tag{2.28}$$

$$C^{(ij)}_{\mathrm{GI}}(l) = \int_0^{\chi_H} d\chi \frac{q^i(\chi)p^j(\chi)}{f^2_{\mathrm{K}}(\chi)} P_{\delta\mathrm{I}}(\frac{l}{f^2_{\mathrm{K}}(\chi)}, \chi). \tag{2.29}$$

With χ_H being the comoving distance to the horizon, $f_{\mathrm{K}}^2(\chi)$ being the comoving angular diameter distance, given by:

$$f_{\mathrm{K}}^2(\chi) = \begin{cases} 1/\sqrt{K}\sin(\sqrt{K}\chi), & \text{if } K > 0 \text{ (open)} \\ \chi, & \text{if } K = 0 \text{ (flat)} \\ 1/\sqrt{K}\sinh(\sqrt{K}\chi), & \text{if } K < 0 \text{ (closed)} \end{cases}, \tag{2.30}$$

where $1/\sqrt{K}$ is the curvature radius of the spatial components of spacetime.
$p^i(\chi) = p^i(z)dz/d\chi$, with $p^i(z)$ the redshift distribution of the galaxies in bin i and $q^i(\chi)$ is the lensing weight function of bin i[23]:

$$q^i(\chi) = \frac{3H_0^2\Omega_m}{2c^2}\frac{f_{\mathrm{K}}^2(\chi)}{a(\chi}\int_{\chi}^{\chi_H} d\chi' p^i(\chi')\frac{f_{\mathrm{K}}^2(\chi'-\chi)}{f_{\mathrm{K}}^2(\chi')}. \tag{2.31}$$

Although these tomographic bins ideally would be separated in redshift, this is always possible. Redshift determination in surveys is not exact and movement of galaxies besides that caused by expansion of space also influence redshifts. Thus, the bins partially overlap. This is further elaborated on in section 6.1.

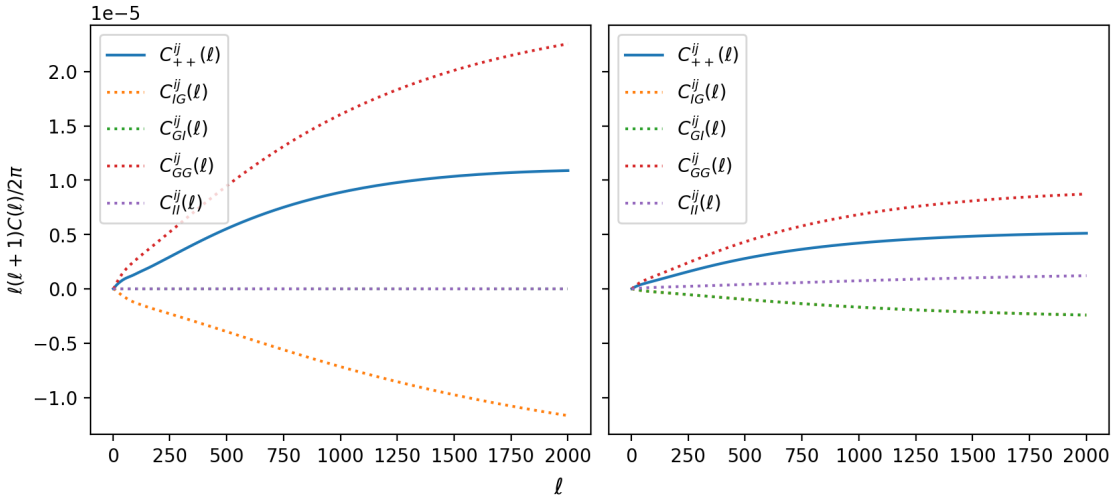

Figure 4: Theoretical predictions for $C_{++}^{(ij)}(l)$ and its components as in equation 2.26. The left image shows the power spectra between two non-overlapping redshift bins i (closer, the lowest redshift bin in figure 19 in section 6.2) and j (further away, the fourth redshift bin in figure 19). he $C_{\mathrm{GI}}^{(ij)}(l)$ and $C_{\mathrm{II}}^{(ij)}(l)$ term overlap as they are both zero. The right image shows the power spectra between galaxies in the lowest redshift bin in figure 19 (in section 6.2) and themselves. The $C_{\mathrm{GI}}^{(ij)}(l)$ and the $C_{\mathrm{IG}}^{(ij)}(l)$ term overlap as they represent the same correlation when $i = j$, as is the case here.

As is clear from equation 2.31, the projected angular power spectra depend explicitly on cosmological parameters. Thus, by measuring the angular power spectra, one could restrict these parameters. Assuming 5 redshift bins, there are 15 unique $C_{++}^{(ij)}(l)$s, so 15 measurable power spectra. If one were to measure 2 shapes per galaxy, this would effectively up the amount of measurable power spectra to 55 instead. Intuitively, having more measurements would mean a very straighforward way to improve our constraining power of cosmological parameters.
However, these $C(l)$s would not be unrelated, as the GG terms will for two $C(l)$s with different shape measurements will be the same. Furthermore, the $C_{\mathrm{GI}}^{(ij)}(l)$ ($C_{\mathrm{IG}}^{(ij)}(l)$) terms will only depend on the shape measurement method of the galaxies in the j (i) bin. Also, when assuming the nonlinear alignment model, the only difference between measurements will be the constant A_{IA} factor, thus not adding any additional information on parameters by itself. However, if one adds cosmic variance to the predictions for measurements, there is value in extra measurements. Since this essentially means remeasuring the lensing measurements,

but with different intrinsic alignment, thus better constraining the lensing effect. We explore this concept in section 6, with the results in section 7.

Part I
Measurement of ΔA_{IA}

The first question we ask is: Are we able to measure a difference in alignment signal between shape measurement methods? To do so, we try to measure the amount of alignment, quantified in A_{IA}, using different shape measurements. Our different shape measurements are sensitive to different areas of the galaxies and we thus expect them to measure different alignment signals. We try to find A_{IA} for our methods and galaxy sample by measuring both w_{g+} and w_{gg}. To reduce the error in the difference between w_{g+} measurements, we also look at $w_{g\Delta+}$, which is the same quantity, just calculated with the difference in ellipticity of a galaxy between two methods instead of the ellipticity of galaxy. To estimate the error in the measurement of these correlations, we use Jackknife error estimation. We then fit the theoretical predictions to the measured projected correlation functions to find A_{IA}, b_g and ΔA_{IA}. To measure this, we use a galaxy catalogue that is a combination of redshift data from the Galaxy And Mass Assembly survey (GAMA) and shape data from the Kilo Degree survey (KiDS). We then select two subsets from this catalogue, where we expect a strong alignment signal.

3 Data

3.1 GAMA

GAMA is a spectroscopic survey, which means the light that enters the telescope gets dispersed and the intensity of light per wavelength can be measured to great accuracy. This means that the redshift of the source can be estimated very accurately by looking at how much the absorption lines of specific elements have been moved. GAMA has a total sky coverage of approximately 286 deg^2, divided into three equatorial regions of 60 deg^2 (G09, G12 and G15) and two southern regions, of 55.7 deg^2 (G02) and 50.6 deg^2 (G23)[24][25]. We only use the equatorial regions, as region G02 does not overlap with our KiDS data and G23 has different target selection. This leaves us with approximately 180 deg^2 and 180 000 galaxies. One important advantage of GAMA is its high completeness, as in the regions used here, the redshift information is obtained for 98.5% of the galaxies.

3.2 KiDS

KiDS is a survey designed for weak lensing, shape and photometric redshift measurements[26][10][27]. The main goal of the survey is mapping the large scale matter distribution in the universe. It is a photometric survey, which means that the light from sources is passed through a filter to only measure a specific part the spectrum at a time. It can measure smaller scales more accurately than spectroscopic surveys however.
KiDS covers 1350 deg^2 with four filters (u, g, r and i) with mean limiting magnitudes 24.23, 25.12, 25.02, 23.68 (5σ in a 2" aperture). Since we are restricted to the regions also covered by GAMA, we still have sky coverage of 180 deg^2 and 180 000 galaxies as before.
One important complication when trying to accurately determine the shapes of light sources is the Point Spread Function (PSF) of a measurement. The PSF quantifies how and how much a point source gets spread out by the atmosphere and the optics of the telescope when it is measured. This means that shapes of sources smaller than the PSF cannot be measured accurately, as one will be measuring the PSF shape instead of the source shape. As our shapes are determined using the r-band filter, we care about the r-band PSF which has a mean size of 0.70" and an average shape $(1 - a/b)$ of about 0.05.

3.2.1 Shape measurement method

The shapes of our galaxies were originally measured in Georgiou et al. (2019)[28] and Georgiou et al. (2019)[29], where they were measured using DEIMOS[30] in the r-band of the KiDS survey. DEIMOS is a moments-based method: it uses the surface brightness moments of a galaxy image to determine its shape. This method allows us to use high-order moments to correct for the weight function (explained later on), which is necessary when the imaging data had a lot of noise. This method also treats the PSF analytically and is limited by how accurately one can model the PSF on the position of the galaxy, not by any assumptions made about the PSF. Lastly, it allows us to vary the radial weight function, to probe different regions of the galaxies, with a larger (smaller) weight function meaning the measurement is more sensitive to the outer (inner) regions. This allows us to compare the intrinsic alignment of different parts of galaxies and ultimately is what helps us constrain ΔA_{IA}.
To explain how this method works, we first need to explain the unweighted moments of the surface brightness distribution $G(\boldsymbol{x})$ of a galaxy, which is expressed by[29]

$$Q_{ij} \equiv \int G(\boldsymbol{x}) x_1^i x_2^j d\boldsymbol{x} \tag{3.1}$$

with $\boldsymbol{x} = x_1, x_2$ the Cartesian coordinates with the galaxy's center as origin.
We can now get the ellipticity of a galaxy from these second order moments:

$$\epsilon = \epsilon_1 + i\epsilon_2 = \frac{Q_{20} - Q_{02} + i2Q_{11}}{Q_{20} + Q_{02} + 2\sqrt{Q_{20}Q_{02} - Q_{11}^2}} \tag{3.2}$$

However, we don't actually measure $G(x)$, we measure $G(x)$ combined with the distortion due to the PSF:

$$G^*(\boldsymbol{x}) = \int G(\boldsymbol{x}') P(\boldsymbol{x} - \boldsymbol{x}') d\boldsymbol{x}' \tag{3.3}$$

where $P(\boldsymbol{x})$ is the PSF kernel. To retrieve the actual shape we use the formula[30]:

$$\{G^*\}_{i,j} = \sum_k^i \sum_l^j \binom{i}{k} \binom{j}{l} \{G\}_{k,l} \{P\}_{i=k, j=k}. \tag{3.4}$$

This means that if want to know G up to a certain order, we would need to know G^* and P up to that same order.
Also, to calculate Q_{ij} we need to integrate over area of the image, which we choose to be large enough to capture the whole galaxy, but which gets dominated by noise far away from galaxy. Thus we need to apply a 2D weight function $W(x)$, centered on the galaxy, to suppress noise at large distance from that center. If we assume this (Gaussian) background noise is there and we weigh the flux, we get:

$$I_w(\boldsymbol{x}) = W(\boldsymbol{x}) I(\boldsymbol{x}) = W(\boldsymbol{x})(G * (\boldsymbol{x}) + N(\boldsymbol{x})), \tag{3.5}$$

where $I_w(\boldsymbol{x})$ is the measured flux, $I(\boldsymbol{x})$ is the flux of the image before weighting, which is equal to $G^*(\boldsymbol{x})$ plus the background noise $N(\boldsymbol{x})$.
We want this weight function to be the same shape as the galaxy so that we exclude as little light from the galaxy as possible and the signal-to-noise is maximised. Because galaxies are approximately elliptical, we choose an elliptical weight function:

$$W(\boldsymbol{x}) = \exp\left[-(\boldsymbol{x} - \boldsymbol{x}_c)^T \begin{pmatrix} 1 - \epsilon_1 & -\epsilon_2 \\ -\epsilon_2 & 1 + \epsilon_1 \end{pmatrix} \frac{\boldsymbol{x} - \boldsymbol{x}_c}{2r_{wf}^2} \right]. \tag{3.6}$$

Here, ϵ_i are the ellipticity components of the weight function, $\boldsymbol{x}_c$ is where the center of the galaxy is and r_{wf} is the scale of the weight function. The ellipticity of the weight function is iteratively tweaked per galaxy, starting from a circular weight, until the signal-to-noise ratio of the measurement converges. Throughout

this tweaking, the area of the weight function is kept the same. Then I_w is deweighted by taking $I = I_w/W$ and Taylor expanding around $\boldsymbol{x}_c$, truncating at order 4, which is stable[29].
A larger r_{wf} means the measurement is more sensitive to the outer regions of the galaxy, while a smaller r_{wf} means the galaxy is more sensitive to the inner regions. r_{wf} is initially chosen to be equal to $r_{iso} = \sqrt{A_{iso}/\pi}$, where A_{iso} is the area of a galaxy's isophote, with the isophote measured at 3σ above the background noise root mean square. A_{iso} is calculated using the ISOAREA_IMAGE parameter from SExtractor[31]. This radius is chosen so that we get good shape signals out of many galaxies.
We then repeat the shape measurements for a few different weight functions with $r_{wf}/r_{iso} = 0.5, 1, 1.5$, to give us an idea of the differences in alignment between methods sensitive to different galaxy regions. To get an idea: $r_{wf}/r_{iso} = 0.5$ is on average roughly equivalent to the half light radius. The distribution of the measured ellipticities using these three weight function radii can be seen in 5. The graph seems to hint at the outside of galaxies being rounder than the inside, but it is not clear-cut.

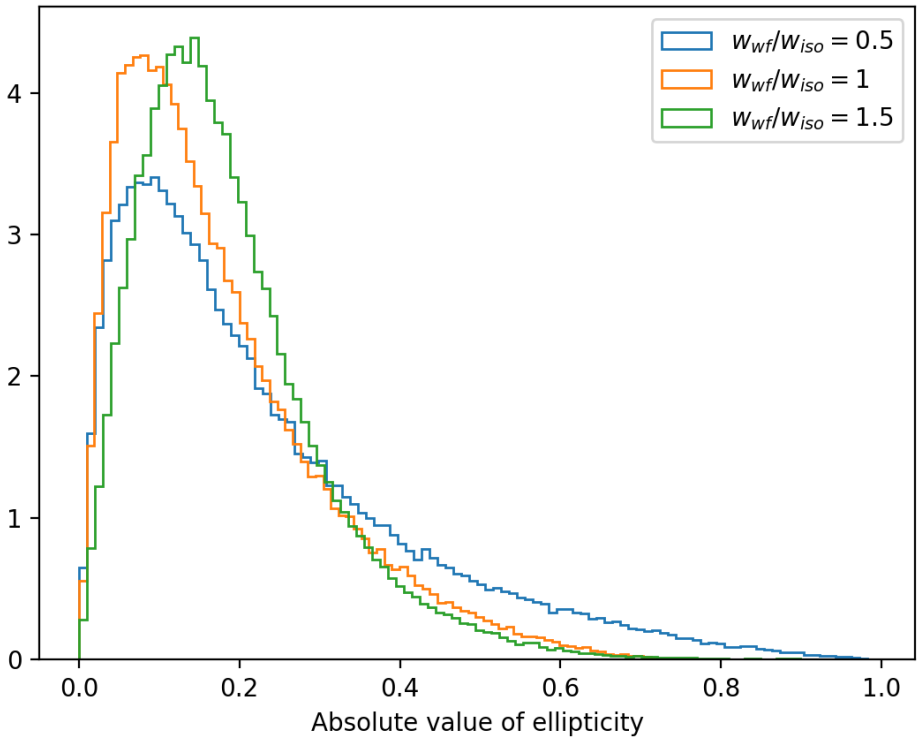

Figure 5: Normalised ellipticity ($= \sqrt{\epsilon_1^2 + \epsilon_2^2}$) distribution for measurements with three different choices of r_{wf}. The ellipticity averages for $r_{wf}/r_{iso} = 0.5, 1, 1.5$ are 0.23, 0.18 and 0.19 respectively.

3.3 Masking

Some areas of our surveys are sadly unusable. The presence of readout spikes, saturation cores, diffraction spikes, primary halos of foreground objects and bad pixels makes it necessary to exclude galaxies in certain regions. We thus apply a mask that removes galaxies near these anomalies, which might impact two-point functions. To negate (part of) that effect, we later construct our measurement methods to include a comparison with a random catalogue, that has a similar distribution as our galaxy catalogue.

3.4 Random catalogue

[32] To accurately measure correlations, we compare them to a random catalogue. The goal of the random catalogue is to remove properties in the survey that are not due to the physics we are interested in, but do influence our measurements. One of the things the randoms need to emulate is structures larger than the survey size, as they cannot be measured but still might influence the scales we do measure[32][20]. Furthermore, the limits of our surveys mean that we see less dim objects further away from us, even if they are physically there, because the amount of their light that reaches us is too small. This means our measurements are biased, which can be negated if our randoms have the same redshift distribution. A comparison of the redshift distribution of the galaxy sample (and two subsamples) and the random sample can be seen in figure 6. Lastly, our removal of certain patches of the sky by masking might also influence two-point correlations, so we need to mask the randoms similarly. The distribution of the brightest 20% of galaxies and their corresponding random clones on patch G09 can be seen in figure 7.

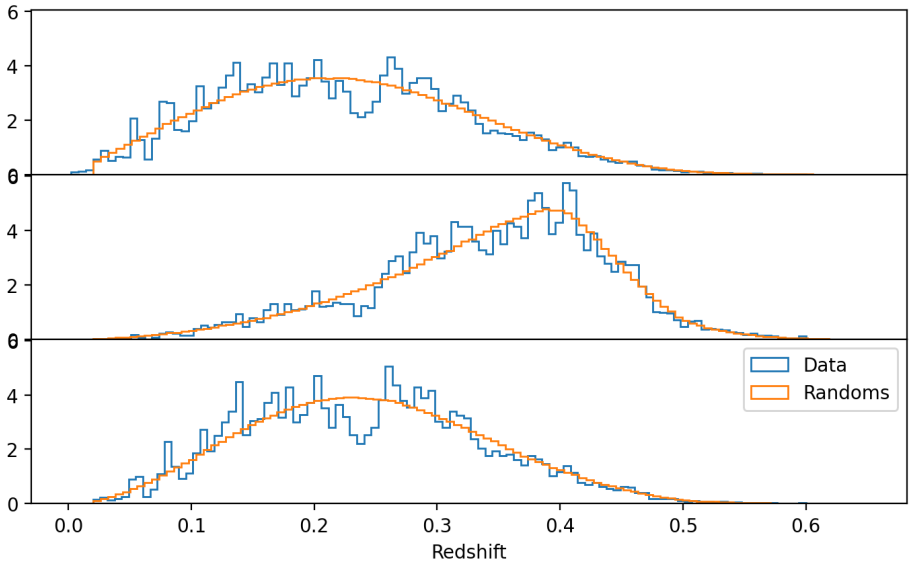

Figure 6: Redshift distributions of the galaxies and their associated randoms. From top to bottom they are the full galaxy sample, the "Brightest" subset and the "Reddest" subset, as defined in section 3.5. The distribution of the "Brightest" subsample is shifted to the right because it excludes the dimmer galaxies only measured at low redshift. The randoms seem to emulate the redshift distribution of the real galaxies well.

We use the random catalogue developed for the GAMA survey[32][1], which is generated based on the Cole method[33]. To generate the randoms, the maximum volume of space over which it could be observed (V_{max}) was found for each galaxy in the survey. V_{max} was calculated by finding the redshift values, z_{min} and z_{max}, for which a galaxy meets the bright and faint magnitude limits of GAMA. The galaxy is then cloned a number of times (on average about 80 randoms per galaxy) and these clones are distributed within a galaxy's V_{max}. These clones have the same stellar mass, absolute magnitude and colour as the original. This forms the basis of the catalogue, where we then mask out the same area as in our galaxy catalogue.

3.5 Data cuts and selection

To obtain good alignment measurements, we first filter out galaxies that are not much larger than the PSF size. We then start selecting galaxies to create a subset where we expect the strongest alignment signal, so that the difference between measurements would also be more prominent. Since many processes in the history of a

[1] http://www.gama-survey.org/dr4/schema/dmu.php?id=109

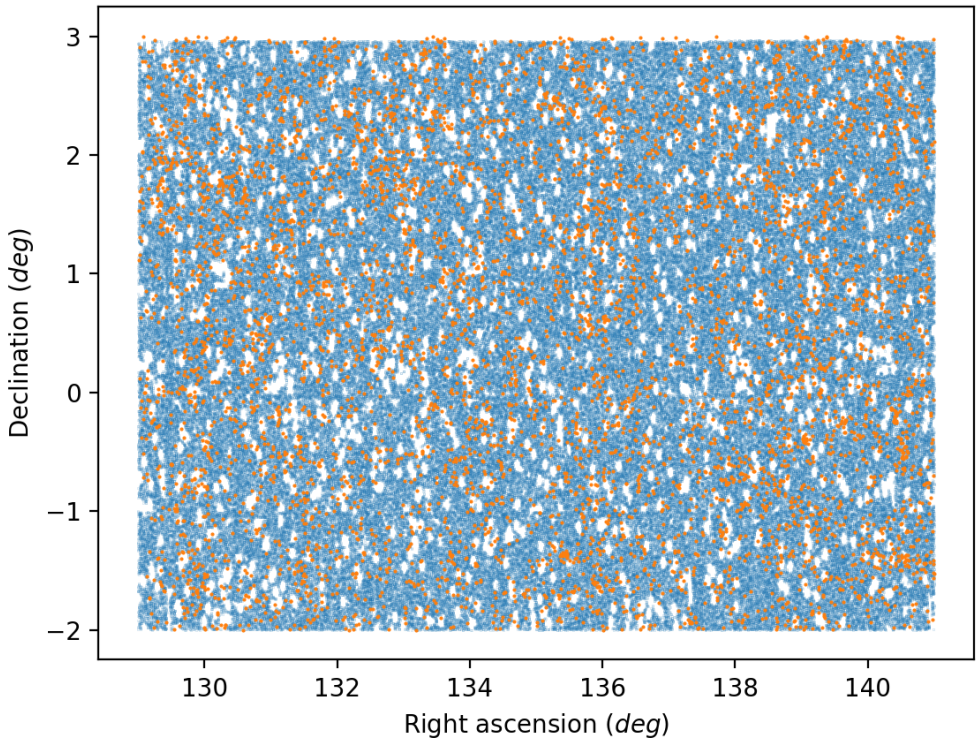

Figure 7: Positions of galaxies (orange) and their associated randoms (blue, 10% the size of orange) in the brightest 20% of galaxies of the G09 patch. The regions where there are no dots mainly indicate regions where the galaxies and the randoms have been masked because accurate measurements for that region could not be obtained.

	Brightest	Reddest
g-i cutoff	0.8	0.95
Brightest %	20	100
Galaxy count (no flags)	20077	77662
Galaxy count (all flags)	18570	67432
Avg r-band luminosity	2.697	1.132
Avg ellipticity ($\frac{1}{2}r_{iso}$)	0.158	0.229
Ellipticity std ($\frac{1}{2}r_{iso}$)	0.118	0.183

Table 1: Table describing the two subsamples that were used. From top to bottom the rows describe: the minimum magnitude in g-i, what percentage of brightest galaxies was selected; the amount of galaxies in the subsample; the amount of galaxies in the subsample with valid shape measurements for all radii used; the average luminosity in the r-band, the average ellipticity measured at a radius of $0.5r_{iso}$; and the standard deviation in ellipticity, measured at a radius of $\frac{1}{2}r_{iso}$.

galaxy can enlarge or decrease its alignment, we can expect the IA signal to depend on a multitude of galaxy properties. However, since we cannot model these effects accurately, we focus on 2 galaxy properties: colour and luminosity. IA seems to be stronger in redder galaxies, which are older and have less star formation[34]. IA also seems to be stronger in more luminous galaxies, Singh et al. (2015)[35] have measured the A_{IA} in the brightest 20% of their galaxies to be 1.7 times as high as in the next 20th percentile.
We thus employ both a colour and a brightness cut. However, taking a strong cut in colour and then taking the brightest 20% of galaxies would have left us with too little to work with, so we employ a more conservative colour cut. This subsample is named "Brightest" in the rest of this thesis.
To be less dependent on our choices here, we have also employed a stronger colour cut and no luminosity cut to obtain a second subsample. This subsample is called "Reddest".
The colour cuts were taken after visual inspection of the distribution of galaxies in the g-i filter-absolute magnitude plane, and estimating where border between the populations of red and blue galaxies was. This distribution, along with the cuts, can be seen in figure 11. Even though we expect a stronger signal for the "Brightest" galaxies, the "Reddest" sample has more than 3 times the amount of galaxies, so it can better help constrain the signal. These numbers and some other properties of the subcatalogues are listed in table 1.

4 Methods

4.1 Estimators

To constrain the difference in A_{IA} between two methods, we look at both w_{g+} and w_{gg}. We can constrain $A_{IA}b_g$ from w_{g+} by fitting measurements to theory and we can find b_g from w_{gg} in a similar matter. Thus, by measuring these two projected correlations, we can find the dependence of the intrinsic alignment on the measurement method. Both of these quantities are measurable in surveys, but the surveys do not cover the full sky, only regions of it. Thus, the influence of structures of larger scale than the survey is there, but not properly measured. Furthermore, not all galaxies in the covered sky region are detected, as some might be not bright enough to detect, making further away dimmer galaxies undetectable. Lastly, even in the covered regions, there exist bright objects that prohibit us from accurately measuring shapes in the full region, more about this in section 3.3.
This means that just measuring the shapes and their correlation alone will give us a biased answer and we must compensate for this. This is done by comparing the measured correlations to a catalogue of randomly distributed similar galaxies[36], where the distribution in brightness, redshift and projected space matches that of the survey. The goal here is to negate survey specific effects as they are not physical, just a consequence of measuring method. This random catalogue is described in section 3.4.
The estimators we used for the true projected correlations as a function of the measured ones are adopted

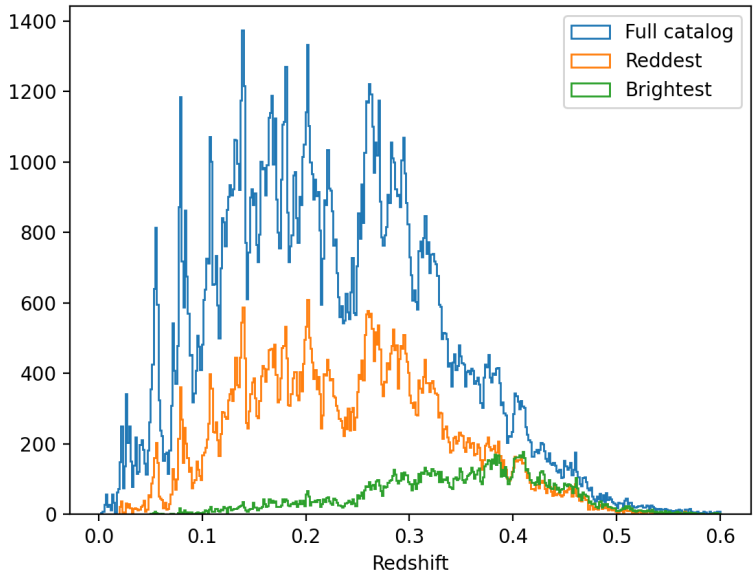

Figure 8: Redshift distribution of the full dataset and the subsets used for analysis.

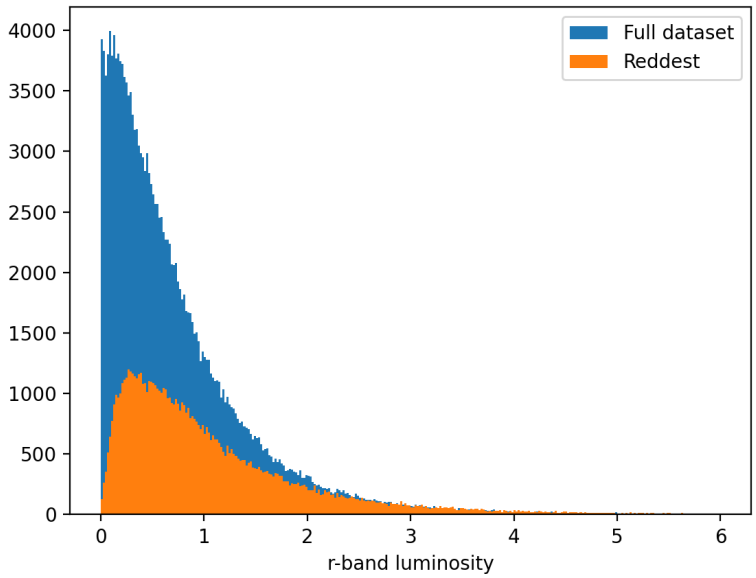

Figure 9: r-band luminosity distribution, compared to an object with an absolute r-band magnitude of -22. The blue bars are the full dataset, the orange bars are the dataset 'Reddest'.

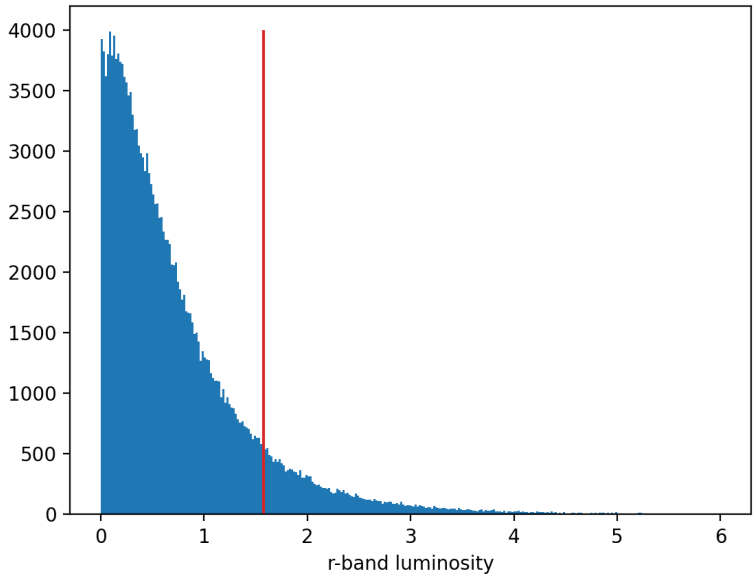

Figure 10: r-band luminosity distribution of the full dataset, compared to an object with an absolute r-band magnitude of -22. The red line indicates the cut for the brightest 20%.

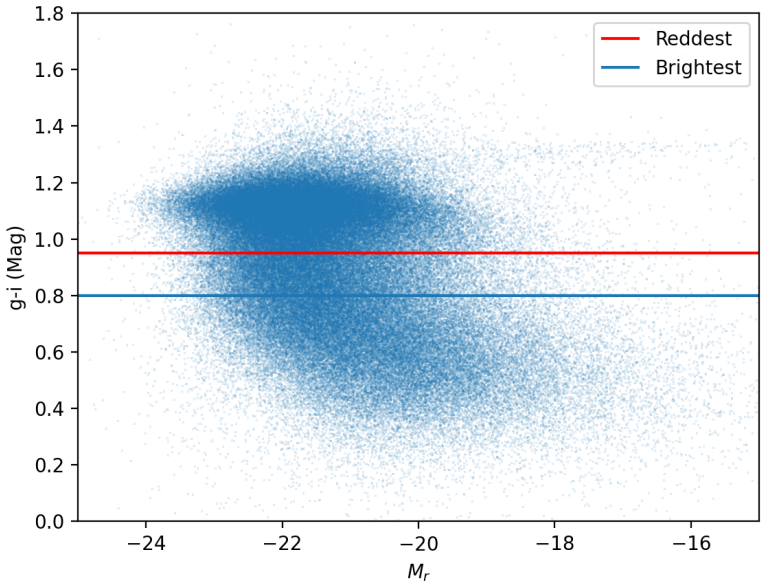

Figure 11: Colour versus absolute magnitude of galaxies in our catalogue. The colour is determined through the difference in magnitude between the light from the source through the g filter and the i filter. The absolute magnitude is taken in the r-band. The lines indicate the two different colour cuts employed to obtain the subsamples we have used in our analysis.

from Mandelbaum et al. (2006)[37]. For the galaxy-intrinsic shear correlation:

$$\hat{\xi}_{g+}(r_p, \Pi) = \frac{S_+D(r_p, \Pi) - S_+R(r_p, \Pi)}{N_{rs}(r_p, \Pi)}. \tag{4.1}$$

Here r_p denotes a projected separation bin with edges $r_p/10^{\Delta log(r_p)/2}$ and $r_p \times 10^{\Delta log(r_p)/2}$ and Π denotes the maximum comoving separation considered. $N_{ab}(r_p, \Pi)$ is the amount of pairs between sample a and b in the bin considered. The r and s signify the random sample and the shape sample. S_+D is

$$S_+D = \sum_{i \neq j | r_p, \Pi} \frac{\epsilon_+(j|i)}{2\mathcal{R}}. \tag{4.2}$$

The sum is over galaxy pairs in the bin, $\epsilon_+(j|i)$ is the ellipticity tangential to the line connecting galaxies j and i, with j in the shape sample and i in the density sample. $\mathcal{R} \approx 1 - \sigma_\epsilon^2$ is the shear responsivity which quantifies how much galaxy ellipticities are affected by gravitational shearing for the galaxy sample used. S_+R is defined the same as S_+D except with the random position sample instead of the galaxy density sample.
We also look at $w_{g\times}$, which is measured through the same estimator as w_{g+}, except with the cross component of the shear instead of the tangential. We expect $w_{g\times}$ to be zero, so we can use this as a test for systematics. For the galaxy-galaxy correlation, we use the Landy and Szalay (1993)[38] estimator:

$$\hat{\xi}_{gg}(r_p, \Pi) = \frac{N_{dd}(r_p, \Pi) - 2N_{dr}(r_p, \Pi) + N_{rr}(r_p, \Pi)}{N_{rr}(r_p, \Pi)}. \tag{4.3}$$

Here d denotes the galaxy position sample.
We project these measurements along the line of sight to make the modelling easier:

$$\hat{w}_{g+}(r_p) = \int_{\Pi_{min}}^{\Pi_{max}} \hat{\xi}_{g+}(r_p, \Pi) d\Pi, \tag{4.4}$$

and similar for w_{gg}.
So by measuring $\hat{w}_{gg}(r_p, \Pi)$ and fitting it to the theoretical prediction as in equation 2.18, we can find b_g^2. Making the reasonable assumption that it can not be negative, we can then fit $\hat{w}_{g+}(r_p, \Pi)$ to equation 2.17 to find $A_{IA} \times b_g$ and thus A_{IA} itself.

4.1.1 Shape difference

To measure the intrinsic alignment difference we use the following estimator:

$$\hat{\xi}_{g\Delta+}(r_p, \Pi) = \frac{S_{\Delta+}D(r_p, \Pi) - S_{\Delta+}R(r_p, \Pi)}{N_{rs}(r_p, \Pi)}, \tag{4.5}$$

with the same binning scheme. $S_{\Delta+}D$ is defined using the difference in ellipticity between the two shape methods considered:

$$S_{\Delta+}D = \sum_{i \neq j | r_p, \Pi} \left(\frac{\epsilon_+^1(j|i)}{2\mathcal{R}^1} - \frac{\epsilon_+^2(j|i)}{2\mathcal{R}^2} \right). \tag{4.6}$$

Here $\epsilon_+^m(j|i)$ is the ellipticity tangential to the line connecting the galaxy pair, measured with shape method m and $\mathcal{R}^m$ is the shear responsivity of the sample, with method m: $\mathcal{R}^m \approx 1 - \sigma_{\epsilon^m}^2$. $S_{\Delta+}R$ is defined similarly. This effectively means that $S_{\Delta+}D = S_{+^1}D - S_{+^2}D$ and thus:

$$\hat{\xi}_{g\Delta+}(r_p, \Pi) = \frac{(S_{+^1}D - S_{+^1}R) - (S_{+^2}D - S_{+^2}R)}{N_{rs}} = \hat{\xi}_{g^1} - \hat{\xi}_{g+^2}. \tag{4.7}$$

So when we project, we obtain:

$$\hat{w}_{g\Delta+}(r_p) = \int_{\Pi_{min}}^{\Pi_{max}} \hat{\xi}_{g\Delta+}(r_p, \Pi) d\Pi = \int_{\Pi_{min}}^{\Pi_{max}} (\hat{\xi}_{g+^1}(r_p, \Pi) - \hat{\xi}_{g+^2}(r_p, \Pi)) d\Pi = \hat{w}_{g+^1}(r_p) - \hat{w}_{g+^2}(r_p). \tag{4.8}$$

This means that we can find the difference in projected intrinsic shape-galaxy position correlation between two measurements by using the same pipeline we use for $\hat{w}_{g+}$, but using $\epsilon_+^1 - \epsilon_+^2$ as the tangential shape measurement. We can then fit this result to the theory for w_{g+} to find $\Delta A_{IA} = A_{IA}^1 - A_{IA}^2$, since in theory $w_{g\Delta+}$ should only differ with a factor from w_{g+}, the shape should stay the same.

4.1.2 Measurement specifics

We have used 30 line of sight separation bins from $-60h^{-1}Mpc$ to $60h^{-1}$Mpc in steps of $4h^{-1}$Mpc and 11 log spaced bins for projected separation between 0.1 and $60h^{-1}$Mpc, following Johnston et al. (2019)[20]. Our estimators were measured using Johnston's 2ptPipeline[2], essentially a wrapper of TreeCorr[39][3].
We have used the same sample for the density and shape catalogue for no other reason than convenience. A future study might want to use a larger density sample to get a decrease in errors.
For individual measurements of w_{g+}, we have used those galaxies that had a clearly resolved shape measurement for the method considered. When calculating $w_{g\Delta+}$ we have only used those galaxies that had good shape measurements for both methods.
Lastly, in practice we have not divided by $\mathcal{R}$ as in equations 4.6and 4.2. Because of the construction of equation 4.6, this cannot be compensated for by a simple division of the end result $w_{g\Delta+}$ with $\mathcal{R}$. Our results are thus 8-12% too big, dependent on the variance of the shape measurement used, but the $\mathcal{R}$ factors approximately cancel when looking at $\Delta A_{IA}/A_{IA}$.

4.2 Jackknife error estimation

Jackknifing is a way to determine the variance and covariance in a measurement when one cannot repeat the experiment multiple times. It takes the full sample, then deletes one 3D patch from it and sees how much the data vector has deviated from the mean. It repeats this for every patch in the data, deleting one at a time, and averages over them. To do this, each patch must be larger than the largest scale under consideration, as to not influence the actual measurement. On the other hand, the amount of patches must be much larger than the data vector, otherwise the errors on the individual data points becomes too large. The jackknife covariance matrix is then estimated by[20]:

$$\hat{C}_{jack} = \frac{N-1}{N}\sum_{a=1}^{N}(\boldsymbol{w}^a - \bar{\boldsymbol{w}})(\boldsymbol{w}^a - \bar{\boldsymbol{w}})^\dagger \tag{4.9}$$

Where N is the number of jackknife regions, w^a is the data vector, measured after excluding region a, $\bar{w}$ is the average value of all w^as and the dagger denotes the transpose conjugate.
We have chosen to adopt similar jackknife regions to Johnston (2019)[20], as they look at the same data with similar tracers. We have chosen for equal-number redhshift subsets with a minimum depth of 150Mpch^{-1}, since the largest line-of-sight separation we look at is $\pm$60Mpch^{-1}. We define 36 regions for our "Brightest" sample and 48 regions for our "Reddest" sample. By comparison: our data vector consists of values in 11 different r_p bins. For a more detailed description of different influences such as masking, we point the reader to Appendix A in Johnston (2019)[20].

5 Results

We present our results using the methods described in the previous section. For both subsets "Brightest" and "Reddest" we have done the following. We have measured the projected correlation function w_{g+} as a function of separation with three different values of r_{wf}. We then fitted theoretical predictions for w_{g+}, as described in equation 2.17, to the smallest radius case, to find $A_{IA}b_g$. To divide out the galaxy bias in these measurements, we have also measured and fitted theoretical predictions (equation 2.18) to w_{gg}. Finally, we have measured $w_{g\Delta+}$ and fitted the predictions for it to it to find ΔA_{IA}. The summary of our results can be seen in table 2. We have solely performed our fits in the range of $r = [6, 30]$Mpc/h. Any lower separations

[2]https://github.com/harrysjohnston/2ptPipeline/
[3]https://rmjarvis.github.io/TreeCorr/

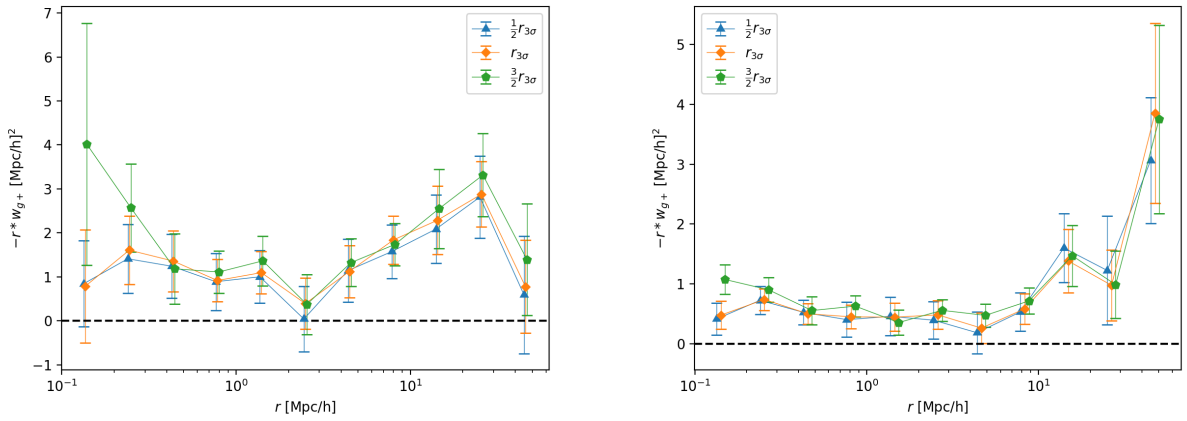

(a) Brightest

(b) Reddest

Figure 12: w_{g+} for the two data subsets, for shape measurements weighted at different ratios from the center of the galaxy (different r_{wf}). Here $r_{3\sigma} = r_{iso}$.

	Brightest	χ^2_{red}	Reddest	χ^2_{red}
b_g	1.19 ± 0.06	1.3	1.03 ± 0.07	1.54
A_{IA} ($\frac{1}{2}r_{iso}$)	1.19 ± 0.64	1.85	4.29 ± 1.38	0.057
ΔA_{IA}	0.55 ± 0.40	1.58	0.86 ± 0.74	0.013

Table 2: A table summarising our results in this section. These are the fitted values for the galaxy bias (b_g), the intrinsic alignment amplitude (A_IA) measured with a weight function with $r_{wf} = \frac{1}{2}r_{iso}$, and the difference in intrinsic alignment amplitude (ΔA_{IA}) between measurements with a weight function with $r_{wf} = \frac{3}{2}r_{iso}$ and with $r_{wf} = \frac{1}{2}r_{iso}$. Also given is the respective reduced χ^2 of the fits.

would be too deep into the nonlinear regime for our approximations of $P_{\delta I}$ and $P_{\delta\delta}$ to be accurate. The higher separation approaches the size of the survey regions and might thus not be properly measured.
As can be seen in figure 12, there is a difference in w_{g+} between weighing ratios. We cannot conclude, however, that this difference is significant, as the errors on our measurements are too large to conclude anything. There does seem to be a hint that the alignment is stronger further from the center, as the higher radius tends to give a higher value than the lower radius.
To constrain the IA amplitude, we first need to constrain the galaxy bias. Measurements for the two samples can be seen in figures 13 and 14, where qualitatively good fits found values of $b_g = 1.03 \pm 0.07$ and $b_g = 1.19 \pm 0.06$ for "Reddest" and "Brightest" respectively.
Our measurements for $w_{g\Delta+}$ can be seen in figures 18 and 16. We again see a trend of the outside of galaxies being stronger aligned, although this trend is not as clear for "Reddest". Our fits are of decent quality, with reduced χ^2 between 1 and 2. If we compare the fitted values for ΔA_{IA} with the fitted values for A_{IA} from the small weight function (in figures 17 and15), we seen a difference of 20% for "Reddest" and 46% for "Brightest". Although our error on all measurements is too big for our results to be called significant, these are upper limits we can work with when considering how multiple shapes might improve analysis of future surveys.

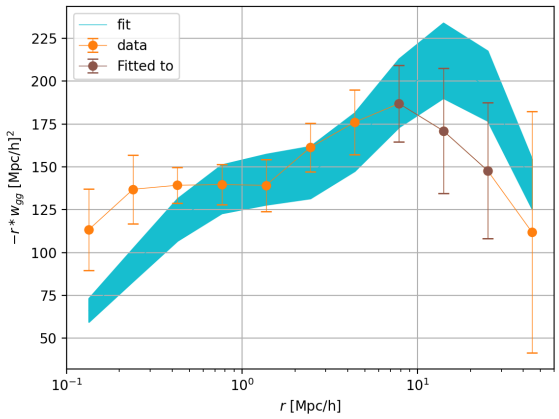

Figure 13: w_{gg} for "Brightest", plus fitted theory with 1 standard deviation interval around it. The fit corresponds to a value of $b_g = 1.19 \pm 0.06$, fitted with $\chi^2_{red} = 1.30$.

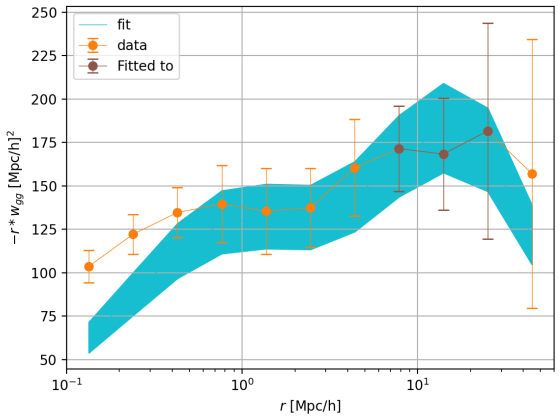

Figure 14: w_{gg} for "Reddest", plus fitted theory with 1 standard deviation interval around it. The fit corresponds to a value of $b_g = 1.03 \pm 0.07$, fitted with $\chi^2_{red} = 1.54$.

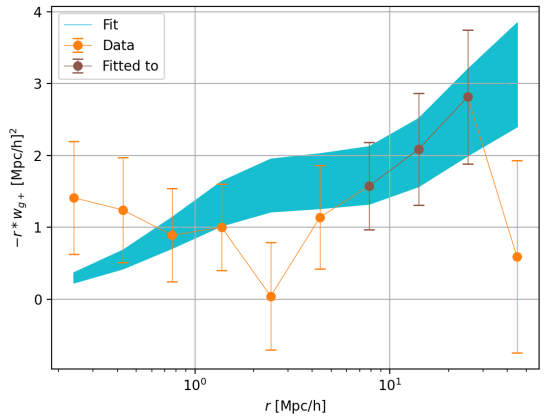

Figure 15: w_{g+} for "Brightest" at $\frac{1}{2} r_{iso}$, plus fitted theory with 1 standard deviation interval around it. The fit corresponds to a value of $A_{IA} * b_g = 1.42 \pm 0.65$, fitted with $\chi^2_{red} = 1.85$.

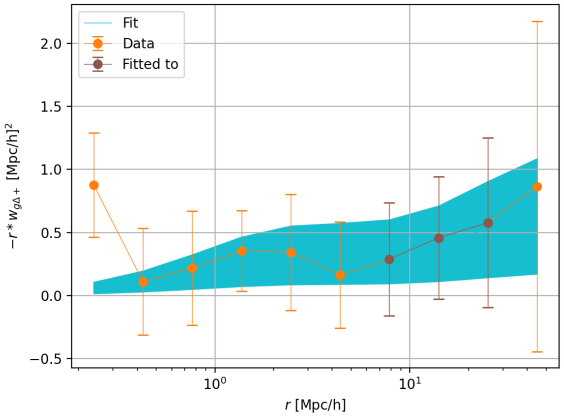

Figure 16: $w_{g\Delta+}$ for "Brightest", plus fitted theory with 1 standard deviation interval around it. The difference is taken between the measurement at $\frac{1}{2}r_{iso}$ and $\frac{3}{2}r_{iso}$. The fit corresponds to a value of $\Delta A_{IA} * b_g = 0.66 \pm 0.42$, fitted with $\chi^2_{red} = 1.58$.

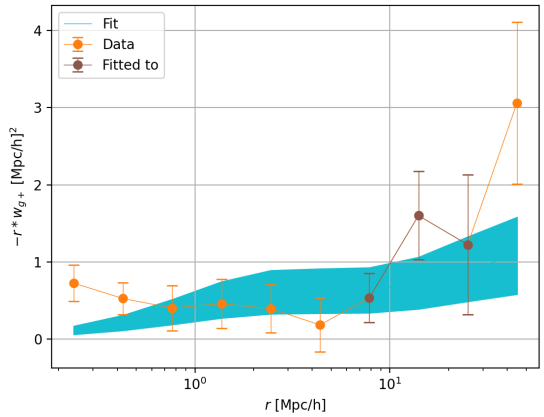

Figure 17: w_{g+} for "Reddest" at $\frac{1}{2}r_{iso}$, plus fitted theory with 1 standard deviation interval around it. The fit corresponds to a value of $A_{IA} * b_g = 4.42 \pm 1.020$, fitted with $\chi^2_{red} = 0.057$.

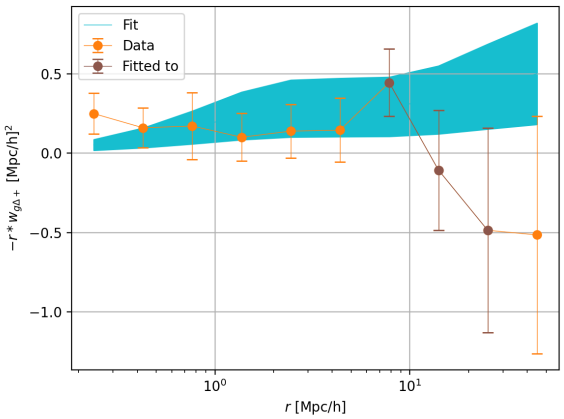

Figure 18: $w_{g\Delta+}$ for "Reddest", plus fitted theory with 1 standard deviation interval around it. The difference is taken between the measurement at $\frac{1}{2}r_{iso}$ and $\frac{3}{2}r_{iso}$. The fit corresponds to a value of $\Delta A_{IA} * b_g = 0.89 \pm 0.65$, fitted with $\chi^2_{red} = 0.013$.

Part II
Forecasting

Now that we have established that there might be a difference in intrinsic alignment between shape measurement methods and that this difference might be measurable, we continue onto our second question: How much would having multiple shape measurements help constrain cosmological parameters? To answer this question we use software to calculate theoretical angular shape-shape power spectra. We generate these in accordance with the expected results of the Legacy Survey of Space and Time[11], which will take place at the Vera C. Rubin Observatory starting 2024. We then calculate the theoretical covariance matrix between these measurements, with an added noise. This noise is correlated between measurements of the same galaxies. We expect this noise to be compensated for with multiple measurements of the same sample. To see how well this improves future results we introduce and employ a variety of measures: the Signal to Noise Ratio, the confidence ellipse, the Figure of Merit and the uncertainty in S_8. To quantify the improvement in the data, we look at the increase in Signal-To-Noise ratio (SNR), increase in a Figure of Merit (FoM) of cosmological parameters, and decrease in the uncertainty in S_8. To obtain the last two, we employ a method called Fisher forecasting. We compare the case where we have two shape measurements with the case where we only use one, to see if having multiple shape measurements is worth it.

6 Methods

The possible extra information gain from multiple shape analysis is especially interesting when considering future surveys such as the Rubin Observatory's Legacy Survey of Space and Time (LSST). LSST aims to cover about 20 000 deg^2, so about half the sky, with a pixel size of 0.2 arcsec per pixel in six different colour bands. It aims to "scan the sky deep, wide, and fast with a single observing strategy, giving rise to a data set that simultaneously satisfies the majority of the science goals"[11]. It will however be a photometric survey, and will thus have less exact redshift measurements than GAMA.

6.1 Data vector

To simulate the upcoming measurements by LSST, we assume measurements of angular tangential shape-tangential shape power spectra $C^{ij}_{++}(l)$, as in equation 2.26, with i and j the galaxy samples being correlated. We consider five different redshift bins, with two shape measurements per bin, effectively giving us 10 galaxy

samples. Since $C^{ij}_{++}(l) = C^{ji}_{++}(l)$, this effectively gives us a data vector of 55 angular power spectra. The way we differentiate between shape measurements in our predictions is by including a different A_{IA} per measurement (A^1_{IA} and A^2_{IA}), where we consider it not to be redshift dependent. This is a realistic assumption at our scales, as no clear redshift dependence before $z_{=}3$ has been found[40] and we do not look much further. We assume $A^1_{IA} = 1$, because this best matches observations when considering a general galaxy population[41], and vary $\Delta A_{IA} = A^2_{IA} - A^1_{IA}$ in the range 0.5-0.85 in steps of 0.05 to see what the influence of different types of measurements would be. We consider values of 0.5 and 1.5 for A^1_{IA} in Appendix A. To compare with, we also separately consider the case where we have the same 5 redshift bins, but only 1 shape measurement per bin. This gives us a data vector of 15 power spectra.
The redshift bins have been distributed following the expected redshift distributions of LSST, as given by Chang et al. (2013)[42]:

$$P(z) = z^{1.24} \exp\left[-\left(\frac{z}{0.51}\right)^{1.01}\right]. \tag{6.1}$$

They were then divided up in 5 regions and convolved to resemble the redshifts that will be measured considering LSST will be a photometric survey. The probability that a galaxy with redshift z has a photometrically measured redshift z_p is given by[43]

$$p_{ph}(z_p|z) = \frac{1-f_{out}}{\sqrt{2\pi}\sigma_b(a+z)} \exp\left[-\frac{1}{2}\left(\frac{z-c_b z_p - z_b}{\sigma_b(1+z)}\right)^2\right] + \frac{1-f_{out}}{\sqrt{2\pi}\sigma_b(a+z)} \exp\left[-\frac{1}{2}\left(\frac{z-c_o z_p - z_o}{\sigma_o(1+z)}\right)^2\right]. \tag{6.2}$$

Where f_{out} is fraction of catastrophic outliers and the other parameters can be tweaked to mimic different cases. Our choices for parameters are the same as in Euclid Collaboration(2020)[43]: $c_b = 1.0$, $z_b = 0.0$, $\sigma_b = 0.05$, $c_o = 1.0$, $z_o = 0.1$, $\sigma_o = 0.05$, $f_{out} = 0.1$.
The redshift distributions can be seen in figure 19. There is some overlap between redshift bins because we do not expect the redshift measurements to be perfect. Photometric redshifts are not as precise as spectroscopic ones and the movement of galaxies with respect to the expanding space will cause some redshift spread as well.
The codes to generate the shape-shape power spectra used the Core Cosmology Library (CCL)[4][6] which essentially integrates equations 2.27 through 2.29 and adds them up. It uses matter power spectra generated through CAMB [44].
These power spectra were generated using cosmology following WMAP9+eCMB+BAO+H_0 as in Hinshaw et al. (2013)[14]. We model the fractional sky coverage and number of galaxies per steradian after LSST from the LSST science book[11] and Chang et al. (2013)[42] respectively. We expect our shape noise to be in accordance with Bhandari et al. (2021)[45]. Note that the galaxy density per steradian is the expected full density, which is optimistic since not all galaxies will have usable shape measurements. The values can be seen in table 3. The power spectra were evaluated over values of $l = 2$ through $l = 2000$ in steps of 1.

6.2 Covariance matrix

To estimate the covariance matrix of the data vector, we use the following formula following[46]:

$$\Sigma^{k,m}_{i,j}(l) = \mathrm{Cov}[C_{i,j}(l), C_{k,m}(l)] = \frac{1}{(2l+1)f_{sky}}(\bar{C}_{i,k}(l)\bar{C}_{j,m}(l) + \bar{C}_{i,m}(l)\bar{C}_{j,k}(l) \tag{6.3}$$

Where $\bar{C}_{i,k}(l)$ is the angular tangential shape-tangential shape power spectrum plus added noise:

$$\bar{C}_{i,k}(l) = C_{i,k}(l) + \delta_{z_i,z_j} corr_{s_i,s_j} \frac{\sigma^2_\epsilon n_z}{2\bar{n}_g}. \tag{6.4}$$

Here i, j are the shape samples being compared, δ_{z_i,z_j} is 1 if i and j are in the same redshift bin ($z_i = z_j$), $corr_{s_i,s_j}$ is 1 if the same shape measurement method is used to generate i and j ($s_i = s_j$, so $A^1_{IA} = A^2_{IA}$)

[4] https://github.com/LSSTDESC/CCL

Quantity	Symbol	Value
Baryon density	Ω_b	0.04628
Matter density	Ω_c	0.2865
Reduced Hubble constant	h	0.6932
Slope of primordial power spectrum	n_s	0.9608
Power spectrum amplitude at 8Mpch^{-1}	σ_8	0.820
Fractional sky coverage	f_{sky}	0.48
Galaxy density per steradian	$\bar{n}_g$	3.1×10^8
Standard deviation in ellipticity	σ_ϵ^2	0.23

Table 3: Table describing the parameters used in the forecasting. The cosmological parameters are taken from Hinshaw et al. (2013)[14], in accordance with WMAP9 plus priors. The survey specific parameters are taken in accordance with the expected values for LSST[11][42][45].

and equal to the correlation between the two shape measurements otherwise, n_z is the number of z bins and σ_ϵ and $\bar{n}_g$ are described in table 3. We have inserted $corr_{s_i,s_j}$ here because the shape noise between two measurements of the same galaxies is physically correlated.
To see what the influence of different types of measurements would be, we consider a range of possible correlations between measurements: 0.5-0.95 in steps of 0.05. We also calculate the correlation between the shape measurements we took the difference between in part I, to see what correlation can be expected.

6.2.1 Signal to Noise Ratio

As a first indication for any improvement in our constraining power, we look at the Signal to Noise Ratio (SNR). This is a measure for the amount of information in our measurements, compared to the uncertainty in those measurements. It was calculated by taking[45]

$$\mathrm{SNR}^2 = \sum_{l=2}^{2000} C^T(l) \cdot \Sigma(l)^{-1} \cdot C(l). \tag{6.5}$$

Here $C^{(T)}(l)$ is the (transposed) data vector and Σ is the covariance matrix of that data vector as defined in equation 6.3.

6.3 Fisher forecasting

To see the improvement in our knowledge of cosmological parameter we use Fisher forecasting. Fisher forecasting is a way to construct the covariance matrix of parameters of interest from a data vector and the covariance matrix of that data vector. The Fisher matrix ($F_{\alpha\beta}$) is defined as the expectation value of the Hessian matrix of the negative log-likelihood of the data vector ($\mathcal{L} \equiv -\ln L$ with L the probability distributions of the elements of the data vector[47]), with respect to parameters of interest (p)[45][47]:

$$F_{\alpha\beta} \equiv \left\langle \frac{\partial^2 \mathcal{L}}{\partial p_\alpha \partial p_\beta} \right\rangle. \tag{6.6}$$

Again, our data vector consists of theoretical predictions for angular power spectra, as functions of l, and the covariance matrix is defined in equation 6.3.Our parameters of interest are Ω_m (the matter density in the universe), Ω_b (the baryon density in the universe), h (the reduced Hubble constant, defined as $H_0/100$), n_s (the scalar spectral index), σ_8 (density fluctuations at $8h^{-1}$Mpc) and the two different values of A_{IA} we expect to measure per galaxy. If the covariance matrix ($\Sigma(l)$) is assumed to be independent of the cosmological parameters and we assume the error in the parameters to be Gaussian (which is not a great approximation), the Fisher matrix can be calculated using[45][23]:

$$F_{\alpha\beta} = \sum_l \frac{\partial C(l)^T}{\partial p_\alpha} \cdot \Sigma(l)^{-1} \cdot \frac{\partial C(l)}{\partial p_\beta}. \tag{6.7}$$

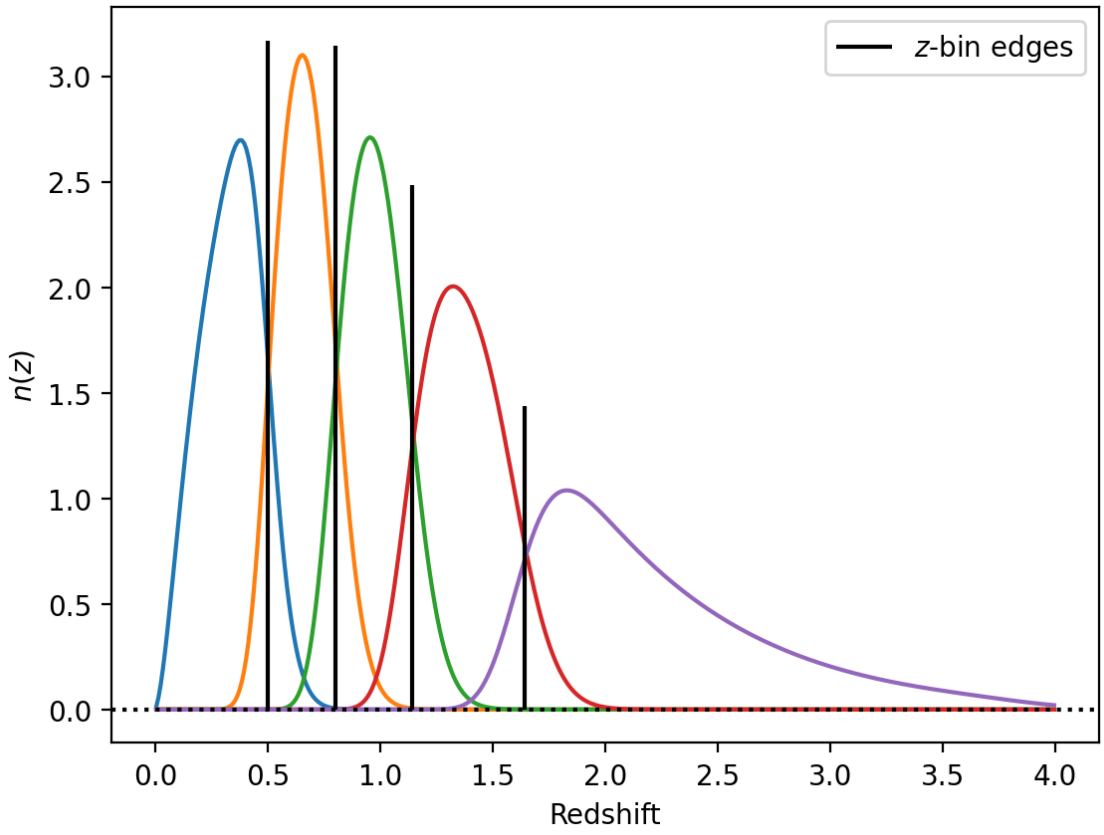

Figure 19: The redshift distribution used to calculate the angular shape-shape power spectra for forecasting. The distribution follows estimations for what LSST will measure[42]. The distribution was split into equal number bins and then convolved to approximate realistic photometric redshift measurements[43].

	$w_{\nu,n}$						
ν	1	2	3	4	5	6	7
$n=3$	$-\frac{1}{2}$	0	$\frac{1}{2}$				
$n=5$	$\frac{1}{12}$	$-\frac{2}{3}$	0	$\frac{2}{3}$	$-\frac{1}{12}$		
$n=7$	$-\frac{1}{60}$	$-\frac{3}{20}$	$-\frac{3}{4}$	0	$\frac{3}{4}$	$-\frac{3}{20}$	$\frac{1}{60}$

Table 4: Table describing the weights $w_{\nu,n}$ to use in the finite differences methods as in equation 6.8 for some values of n. They are calculated in accordance with Fornberg (1988)[48]. Only uneven values of n are valid and values for $w_{\nu,n}$ with $\nu > n$ are irrelevant as they do not appear in the sum.

The resulting Fisher matrix is the inverse of the covariance matrix of the parameters of interest p and can be used to calculate a variety of indicators of how well constrained the parameters are. The three indicators used in this paper are the Figure of Merit (FoM) in Ω_m and σ_8, the confidence ellipse of these parameters and the standard deviation in S_8 (which is a function of Ω_m and σ_8). These parameters are of specific interest to us because lensing is most sensitive to these parameters, as they describe (part of) the matter power spectrum.

6.3.1 Numerical derivatives

To obtain the Fisher matrices, we need to take derivatives of $C_{i,j}(l)$ with respect to cosmological parameters. Although the relation is relatively clear in some cases, in other cases the dependence is hidden away in the matter power spectrum. We thus take numerical derivatives instead. These partial derivatives were computed using the finite differences methods[48]. This method approximates a partial derivative with respect to a variable x by slightly varying x around the value we are interested in, weighing the outcomes and adding them. The generic formula (for first order derivatives) is

$$\left.\frac{\partial f}{\partial x}\right|_{x=x_0} \approx \sum_{\nu=1}^{n} w_{\nu,n} f\left(x_0 \times (1 + \Delta s(\nu + \frac{1-n}{2}))\right). \tag{6.8}$$

Here x_0 is the value of x we want to know the derivative at, n is the amount of points around x_0 we are evaluating the derivative at (the amount of steps), Δs is the step size as a percentage of x_0 (normalised step size) and $w_{\nu,n}$ is the weighting, which is a function of ν and n, the values of which can be seen in table 4. To see whether the choice of these Δs and n impact our results, we have found C_{ij} to be stable for different combinations of $n = \{3, 5, 7\}$ and $\Delta s = \{0.1, 0.01, 0.001\}$. Since results seem to be stable with respect to our choices, we choose $\Delta s = 0.01$ and $n = 5$ for the rest of our analysis.
As a test, we have also compared the derivative of the angular intrinsic shape-intrinsic shape power spectrum (II) with respect to A^1_{IA}, with the same angular power spectrum, but divided by A^1_{IA}. Since C_{II} should be linear in A^1_{IA}, these two should be the same. They are, as can be seen in figure 20, thus our method seems to work

6.3.2 Confidence ellipses

Confidence ellipses are a good way to visualise the uncertainty in and the covariance between two parameters. They show the contour of a certain confidence in the 2-parameter space and can be calculated using Fisher matrices. We use these to visualise the improvement in our knowledge of Ω_m and σ_8 when considering multiple shape measurements. The steps to get to these ellipses follows the Fisher matrices and confidence ellipses quick start guide by Coe[49].
To get the contours, we need the reduced covariance matrix: the covariance matrix of just our two parameters. We do this by first inverting the Fisher matrix to get the covariance matrix and then marginalising over all parameters except Ω_m and σ_8. This is done by simply removing all rows and columns from the covariance matrix besides the ones pertaining to our 2 parameters. This is akin to integrating over the other parameters, so they are allowed to take any value[49]. We now have a covariance matrix of Ω_m and σ_8 C:

$$C = \begin{pmatrix} \sigma_x^2 & \sigma_{xy} \\ \sigma_{xy} & \sigma_y^2 \end{pmatrix} = \begin{pmatrix} \sigma^2_{\Omega_m} & \sigma_{\Omega_m \sigma_8} \\ \sigma_{\Omega_m \sigma_8} & \sigma^2_{\sigma_8} \end{pmatrix}. \tag{6.9}$$

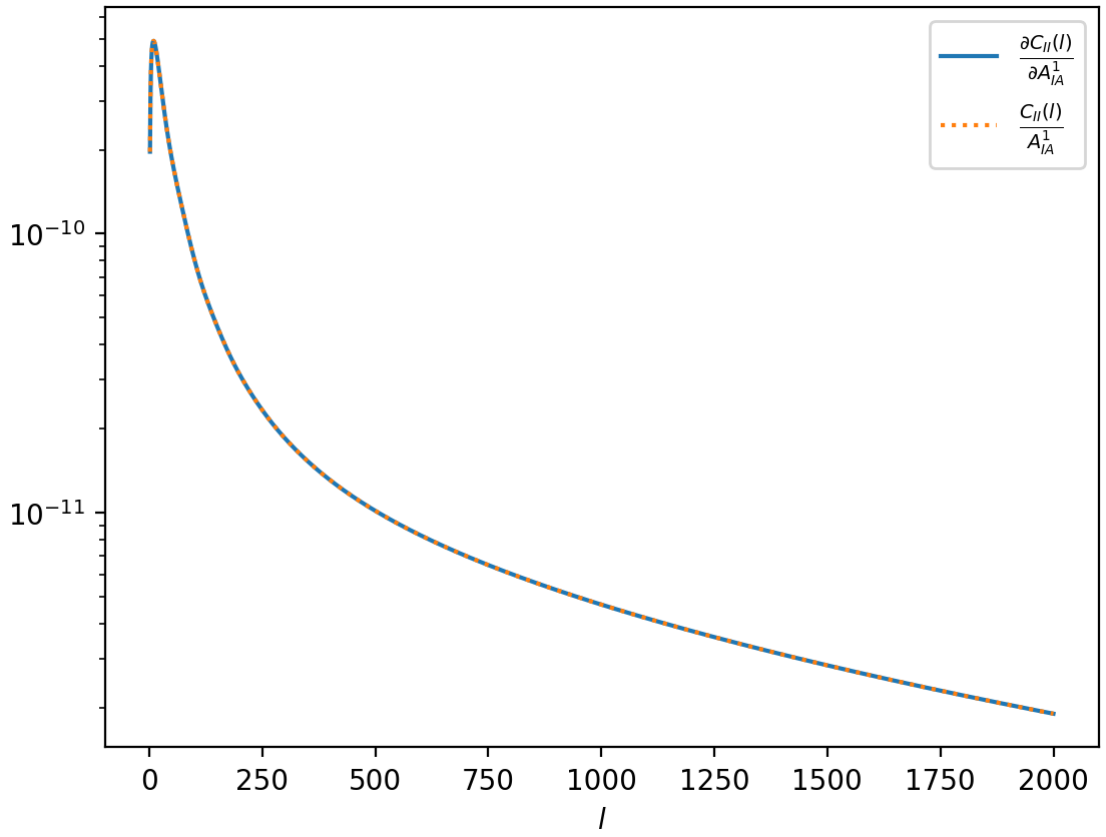

Figure 20: A graph testing the numerical derivative method. One line shows the derivative of the angular intrinsic shape-intrinsic shape power spectrum (II) with respect to A^1_{IA}. The other line shows the same angular power spectrum, but divided by A^1_{IA}. Both galaxy samples for both resided in the same redshift bin (the first in figure 19) and had two different shape measurements with $A^1_{IA} = 0.$ and $A^2_{IA} = 1.$ Since $C_{II}(l)$ in this case is expected to be linear in A^1_{IA}, we expect the two lines to be the same, as is the case.

Note that σ_x^2 and σ_y^2 are defined as squares while σ_{xy} is not. We can now calculate the parameters of the ellipse:

$$a^2 = \frac{\sigma x^2 + \sigma y^2}{2} + \sqrt{\frac{(\sigma x^2 - \sigma_y^2)^2}{4} + \sigma_{xy}^2} \tag{6.10}$$

$$b^2 = \frac{\sigma x^2 + \sigma y^2}{2} - \sqrt{\frac{(\sigma x^2 - \sigma_y^2)^2}{4} + \sigma_{xy}^2} \tag{6.11}$$

$$\tan 2\theta = \frac{2\sigma_{xy}}{\sigma_x^2 - \sigma_y^2}. \tag{6.12}$$

Here a and b are the axis lengths and θ is the angle at which the ellipse should be rotated with respect to the x-axis. We then multiply a and b with a coefficient that depends on what confidence level we are interested in. If we want to show the 1, 2, or 3 standard deviation confidence ellipses, we have to multiply by 1.52, 5.48, 3.41 respectively. We only show the 1 standard deviation ellipses in our plots.

6.3.3 Figure of merit

One way to quantify some of the information of the confidence ellipse is by looking at the area of the ellipse. The larger the uncertainty in the parameters, the larger the area is. Analogous to the Dark Energy Task Force (DETF) Figure of Merit (FoM)[50], we define our own FoM. The DETF FoM is equal to π times the inverse of the area of the 95% confidence ellipse in the $w_0 - w_a$ plane, where w_0 and w_a are parameters for the equation of state of Dark Energy. The larger this FoM, the greater the projected accuracy of the experiment. We define our FoM as the same quantity, but in the Ω_m, σ_8 plane. One way to calculate this is via:

$$\text{FoM} = \sqrt{\det F^{\Omega_m \sigma_8}}, \tag{6.13}$$

where $F^{\Omega_m \sigma_8}$ is the reduced Fisher matrix, the inverse of the reduced covariance matrix we used for the confidence ellipse.

6.3.4 Uncertainty in S_8

A popular way to combine Ω_m and σ_8 is through the quantity S_8, the weighted amplitude of matter fluctuations in the late universe and thus a measure of the homogeneity of the universe. It is defined as

$$S_8 = \sigma_8 \sqrt{\Omega_m / 0.3}. \tag{6.14}$$

There exists a tension in its value however, as Cosmic Microwave Background (CMB) surveys have measured it to be 0.831 ± 0.015[17] and 0.828 ± 0.026[14], but cosmic shear surveys have measured it to be 0.776 ± 0.017[16]. We are thus interested to see whether our methods could help alleviate or clarify that tension.
To see how well we can constrain S_8, we look at the predicted uncertainty in S_8. To do that, we need to transform our Fisher matrix to be in terms of S_8. Since S_8 is only a direct function of Ω_m and σ_8, we first marginalise the covariance matrix as before and invert to get the reduced Fisher matrix. We then transform to get our new Fisher matrix $F^{\Omega_m S_8}$ as follows:

$$F^{\Omega_m S_8} = M^T F^{\Omega_m \sigma_8} M, \tag{6.15}$$

with $F^{\Omega_m \sigma_8}$ the reduced Fisher matrix and $M^{(T)}$ the (transposed) transformation matrix, given by:

$$M = \begin{pmatrix} \frac{\partial \Omega_m}{\partial \Omega_m} & \frac{\partial \Omega_m}{\partial S_8} \\ \frac{\partial \sigma_8}{\partial \Omega_m} & \frac{\partial \sigma_8}{\partial S8} \end{pmatrix} = \begin{pmatrix} 1 & \frac{0.6}{\sigma_8}\sqrt{\frac{\Omega_m}{0.3}} \\ -\frac{1}{2}\frac{\sigma_8}{\Omega_m} & \sqrt{\frac{0.3}{\Omega_m}}. \end{pmatrix} \tag{6.16}$$

By inverting the resulting $F^{\Omega_m S_8}$, we find the covariance matrix that includes $\sigma_{S_8}^2$ as its bottom right element.

7 Results

We present our results showing the improvement in constraining power when using two shape measurements versus when using one shape measurement per galaxy. We present our results for a range of possible correlations between the measurements and for a range of possible differences in measurements. We start our results off by showing the increase in SNR, when comparing two shape measurement methods with one shape measurement method. This can be seen in figure 21. Although the SNR increases for every combination of parameters, it is only a marginal increase for most combinations. SNR increases with lower correlation, which makes sense, as lower correlation means a lower entry in the covariance matrix of the data vector and thus a higher SNR. The influence of ΔA_{IA} is less clear, but can be seen slightly better by looking at figure 22. This plot shows the increase in SNR, normalised per row. It shows that there is some influence of ΔA_{IA}, but it is not clear to us how SNR is influenced exactly.

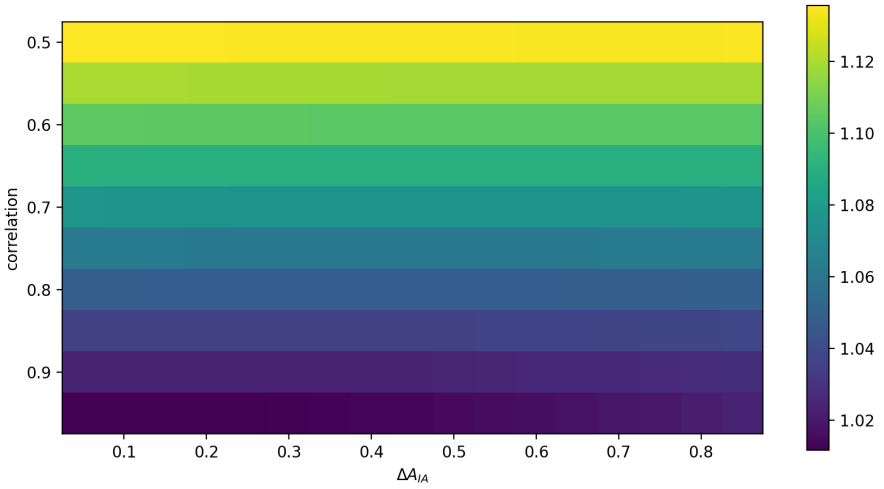

Figure 21: Improvement in the Signal to Noise Ratio of the predicted data for 2 shape measurements, divided by the same quantity for 1 shape measurement. The best improvement is in $(\Delta A_{IA}, corr) = (0.5, 0.1)$, where there is a 14% increase. The realistic values measured in "Brightest" and "Reddest" at $(\Delta A_{IA}, corr) = (0.45, 0.75)$ and $(\Delta A_{IA}, corr) = (0.2, 0.8)$ are 6% and 5% better compared to the 1 measurement case.

We now look at some confidence ellipses. We compare the confidence ellipse for 1 shape measurement with that for 2 shape measurements for 3 pairs of variables. These pairs correspond to the two measured values for ΔA_{IA} in section 5 and one ideal case. They can be seen in figures 23a, 23b and 23c and combined in figure 24. Although the difference is visually marginal for the "Brightest" and the "Reddest" case, there is noticeable improvement in the contours. The 2 A_{IA} ellipses also seem to have turned very slightly towards the x-axis, compared to the 1 A_{IA} ellipses, meaning that our knowledge Ω_m is slightly more improved than our knowledge of σ_8. The two cases imitating our measurements seem to yield very similar results in every regard. For the ideal case, there is a significant reduction in the area of the confidence ellipse.
To further quantify our improvements in constraining power, we turn to the FoM next. As can be seen in figure 26, there is a decent amount of improvement when considering two shapes. There seems to be a preference for higher correlation, as that means the shape noise can be cancelled more effectively, and higher ΔA_{IA}, which means the two measurements are probing different power spectra. In the cases closest to our measurements, the improvements of the FoM when compared to the one shape case are 22% and 29%. In the best case scenario, there is a 75% increase. Even in the worst case, there is a 16% increase in the FoM.
To see whether having multiple shapes can help alleviate or narrow down the S_8 tension, we finally look at the decrease in uncertainty in σ_8, which can be seen in figure 25. This figure follows the same trends as the FoM, which makes sense since the quantities plotted are very much related. Here, the same logic seems to apply that higher correlation allows for more effective noise cancelling and higher ΔA_{IA} probes

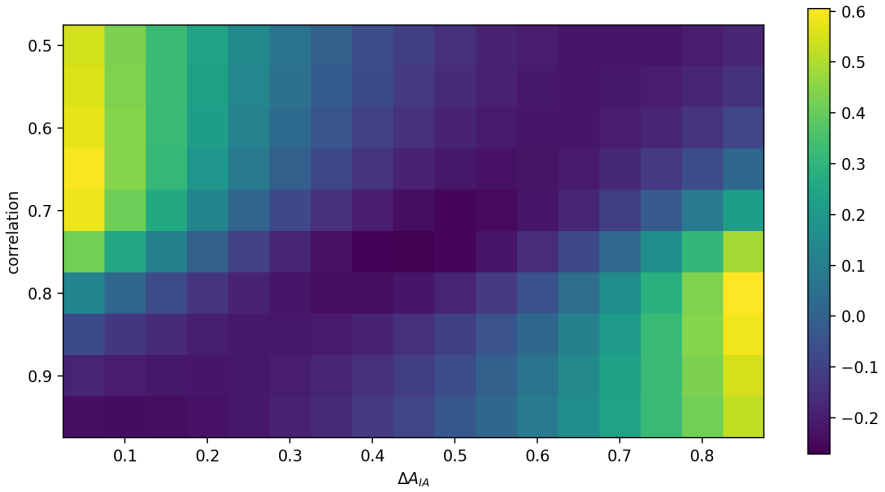

Figure 22: Improvement in the Signal to Noise Ratio of the predicted data for 2 shape measurements, divided by the same quantity for 1 shape measurement. This graph is normalised per row, so it should be interpreted as deviation from the norm, per row. This graph shows there is dependence on ΔA_{IA}, it is just less strong.

different power spectra more effectively. The realistic cases are 20% and 15% better at constraining S_8, and the most optimistic scenario would see an improvement of 35% . The worst case scenario would still mean an improvement of 13%.

Part III
Conclusion

Cosmology still has large open questions about the nature of the universe. Some of these can be answered using galaxy shape correlations, which are a combination of gravitational lensing effects and intrinsic alignment. The intrinsic alignment is dependent on the shape measurement method used, and the correlation functions are thus as well. We looked at the influence of the shape measurement method on intrinsic alignment and how having multiple shape measurements could help constrain cosmological parameters.

In part I of this thesis, we have measured the projected correlation functions between galaxy position and galaxy position, galaxy shape and galaxy position, and difference in galaxy shape and galaxy position in the GAMA+KiDS survey. We have done this using multiple different weighting functions, resulting in multiple shape measurements of the same galaxies. We have done this to then fit theoretical predictions to the correlation functions to find A_{IA} and ΔA_{IA}. We were not able to accurately quantify the difference in intrinsic alignment between the shape measurements. We have, however, provided motivation and an upper limit for our second part.

In part II of this thesis, we have used theoretical predictions for angular power spectra to obtain predictions for how much future surveys could be improved by using multiple shape measurements. This was done by emulating data from the upcoming LSST survey and calculating predictions for the shape-shape angular power spectra. These power spectra were calculated between 5 different redshift bins, with 2 shape measurements each and combined with a theoretical covariance matrix that included correlated noise. We then used Fisher analysis to predict the future gain in uncertainty in S_8. Our results were promising, as even in worst case scenarios, we saw improvements of more than 13% and even higher in realistic scenarios, even up to 35%.

We thus conclude that using multiple shape measurements per galaxy can help improve cosmological constraints, without extra telescope observation time, and should be considered in future analyses.

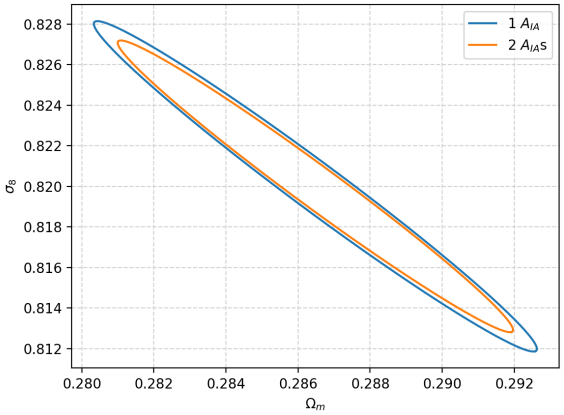

(a) $\Delta A_{IA} = 0.45$ and $corr = 0.75$ in accordance with our "Brightest" measurement.

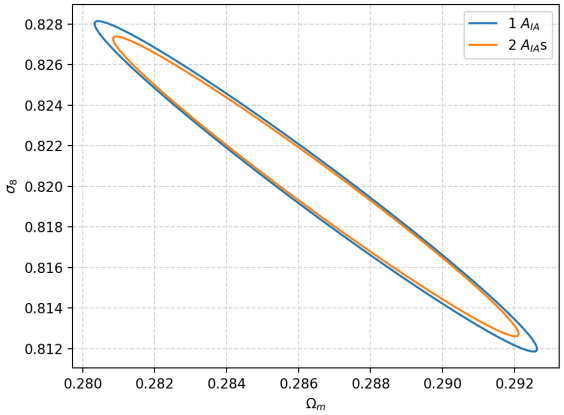

(b) $\Delta A_{IA} = 0.2$ and $corr = 0.8$ in accordance with our "Reddest" measurement.

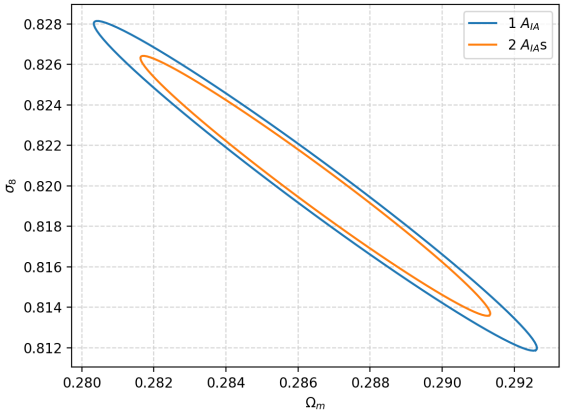

(c) $\Delta A_{IA} = 0.5$ and $corr = 0.95$, which is where we see the most improvement in FoM.

Figure 23: Confidence ellipse of one standard deviation uncertainty in Ω_m and σ_8 with 1 shape measurement compared to the same ellipse with 2 shape measurements.

Future research might be aimed at the scenario where we have an accurate model of A^2_{IA} as a function of A^1_{IA}. As can be seen in figure 27, there might be significant improvement if this relation is accurately modeled, although this plot is preliminary.
Further future research could actually apply these multiple shapes to the LSST survey when it releases, although its first light will be in 2024, so this will have to wait.
Lastly, one might want to redo the measurements in part I of this thesis, but using a bigger density tracer sample. We have used the same sample for the galaxy positions as the galaxy shapes, but one can improve on the errors in the result by including more galaxy positions. Also, we have not divided by the responsivity when calculating the correlation estimators, and ours are thus off by a few percent.

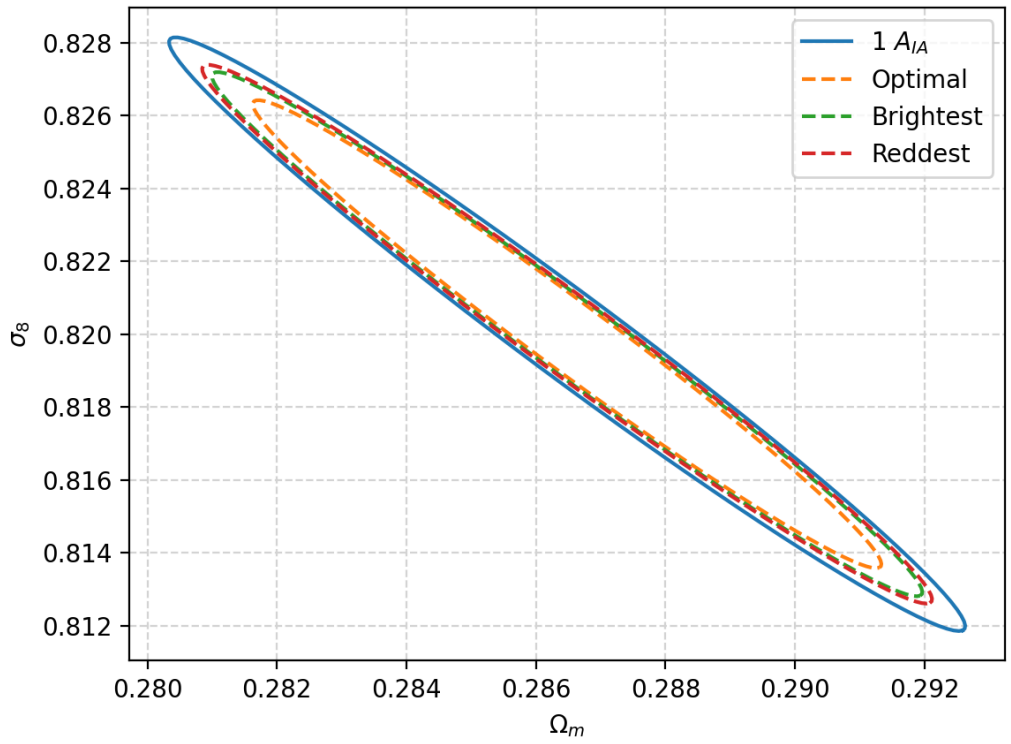

Figure 24: Confidence ellipse of one standard deviation uncertainty in Ω_m and σ_8 with 1 shape measurement compared to the same ellipse with 2 shape measurements, for three different combinations of ΔA_{IA} and $corr$. The chosen values are in accordance with our "Brightest" and "Reddest" measurements, and where we see the most improvement in Fom (called Optimal here). They are the same ellipses as in figure 23, but in one plot.

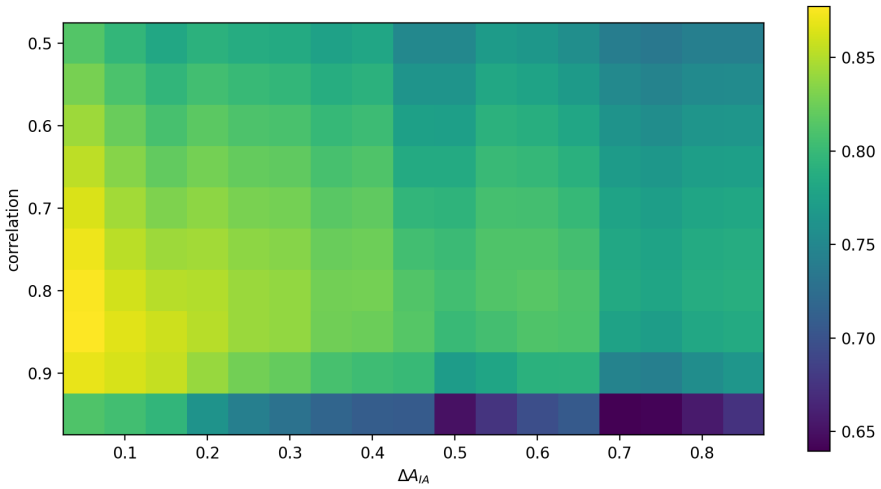

Figure 25: Improvement in uncertainty in S_8 for 2 shape measurements, divided by the same quantity for 1 shape measurement. The best improvement is in $(\Delta A_{IA}, corr) = (0.7, 0.95)$, where there is a 35% decrease. The realistic values measured in "Brightest" and "Reddest" at $(\Delta A_{IA}, corr) = (0.45, 0.75)$ and $(\Delta A_{IA}, corr) = (0.2, 0.8)$ are 20% and 15% better compared to the 1 measurement case.

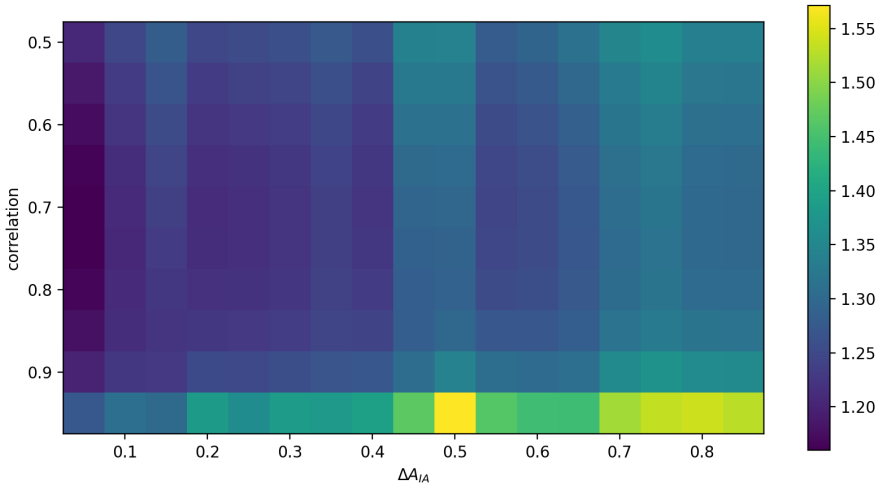

Figure 26: Improvement in the Figure of Merit of Ω_m and σ_8 for 2 shape measurements, divided by the same quantity for 1 shape measurement. The best improvement is in $(\Delta A_{IA}, corr) = (0.5, 0.95)$, where there is a 75% increase. The realistic values measured in "Brightest" and "Reddest" at $(\Delta A_{IA}, corr) = (0.45, 0.75)$ and $(\Delta A_{IA}, corr) = (0.2, 0.8)$ are 29% and 22% better compared to the 1 measurement case.

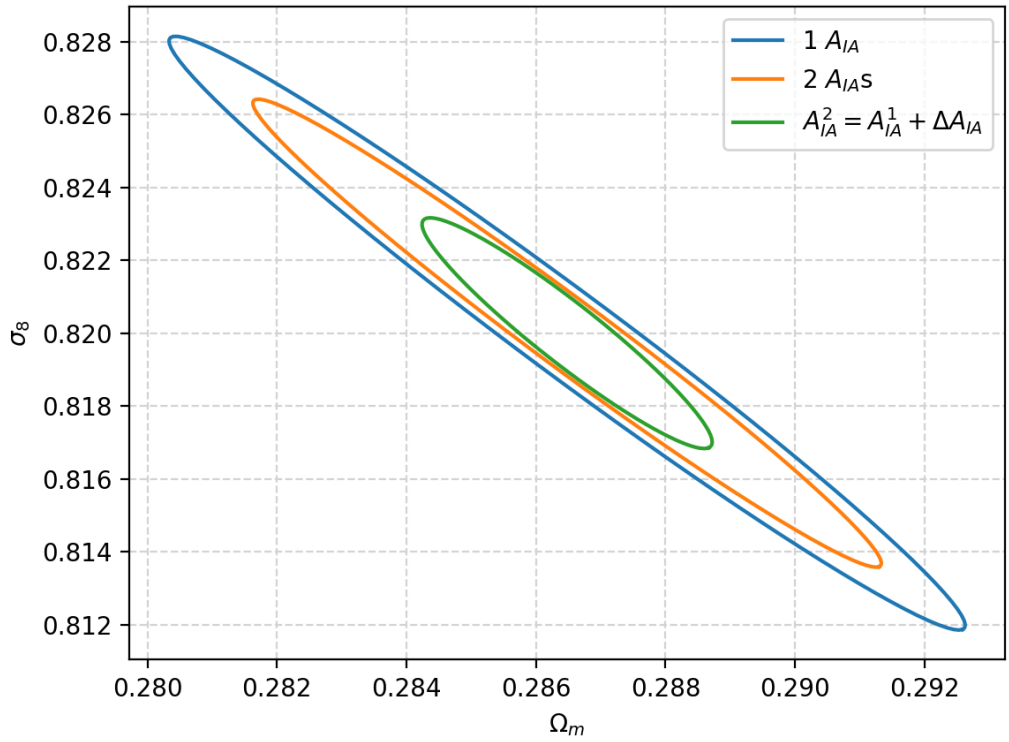

Figure 27: Confidence ellipse of one standard deviation uncertainty in Ω_m and σ_8 with 1 shape measurement compared to the same ellipse with 2 shape measurements and the same ellipse for 2 shape measurements, if we were to know the relation between the intrinsic alignment amplitudes. $\Delta A_{IA} = 0.5$ and $corr = 0.95$. Preliminary result, the methods used were not understood well.

A Appendix

Same graphs as in section 7, but with A_{IA}=0.5 and 1.5. We see that the same trends generally apply for A_{IA}=1.5, with better results with higher ΔA_{IA} and higher correlation, except for in SNR. We do note that the preference for higher ΔA_{IA} is not clear in the case that A_{IA}=0.5, but the preference for higher correlation is there. We do not pose any theories as to what the relation between the Fom, $\sigma(S_8)$ or SNR is with A^1_{IA}.

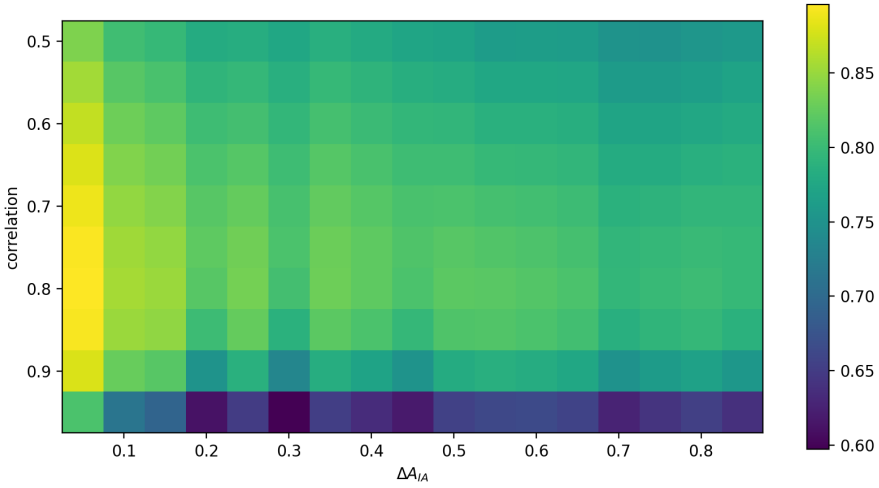

Figure 28: Improvement in uncertainty in S_8 for 2 shape measurements, divided by the same quantity for 1 shape measurement. Now AIA1=0.5.

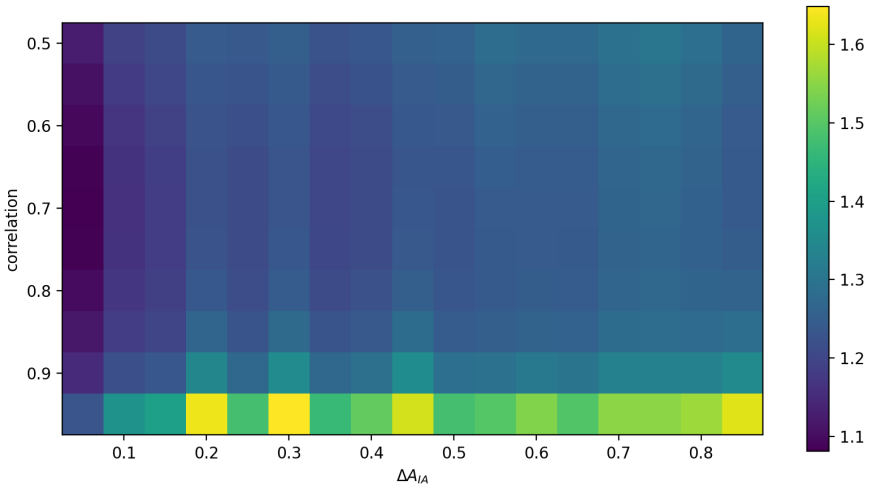

Figure 29: Improvement in the Figure of Merit of Ω_m and σ_8 for 2 shape measurements, divided by the same quantity for 1 shape measurement. Now AIA1=0.5.

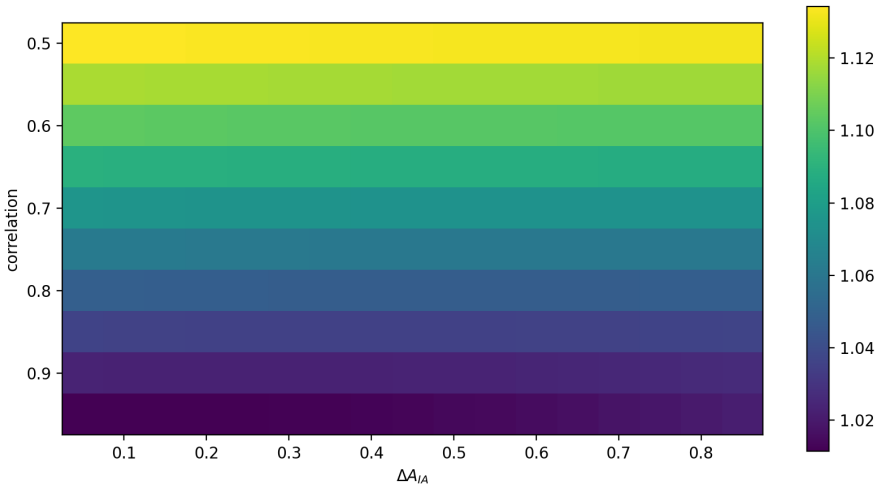

Figure 30: Improvement in the Signal to Noise Ratio of Ω_m and σ_8 for 2 shape measurements, divided by the same quantity for 1 shape measurement. Now AIA1=0.5.

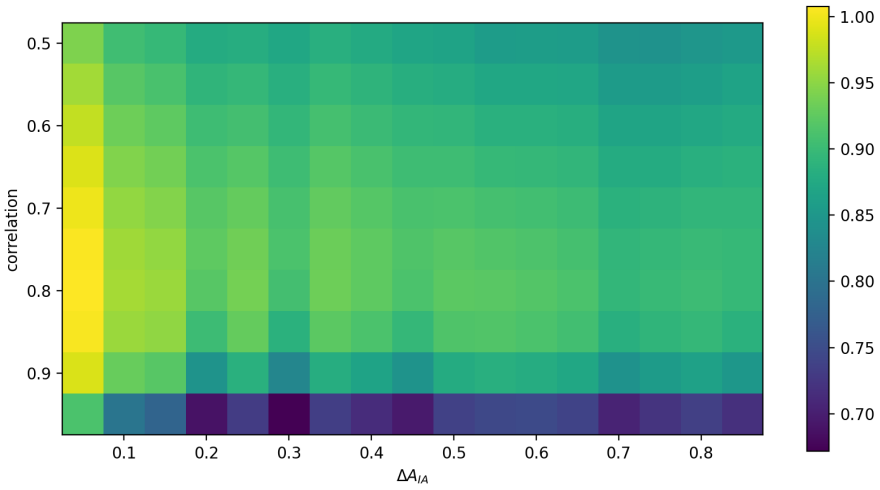

Figure 31: Improvement in uncertainty in S_8 for 2 shape measurements, divided by the same quantity for 1 shape measurement. Now AIA1=1.5.

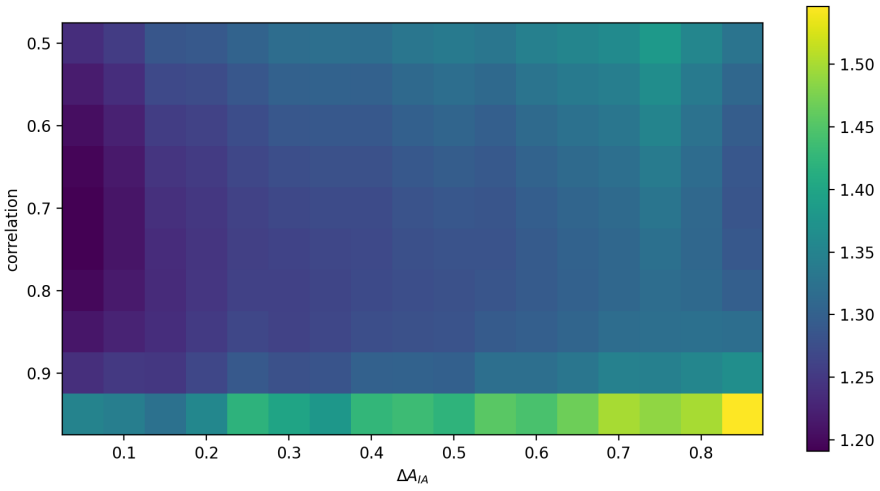

Figure 32: Improvement in the Figure of Merit of Ω_m and σ_8 for 2 shape measurements, divided by the same quantity for 1 shape measurement. Now AIA1=1.5.

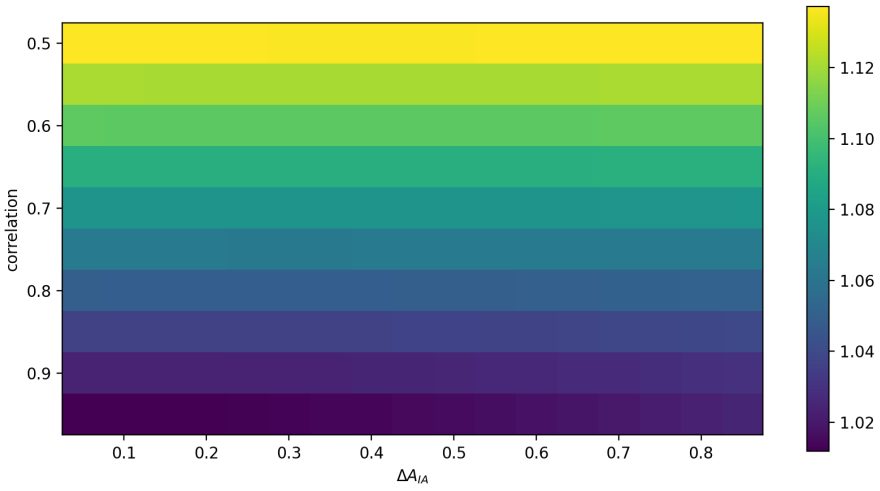

Figure 33: Improvement in the Signal to Noise Ratio of Ω_m and σ_8 for 2 shape measurements, divided by the same quantity for 1 shape measurement. Now AIA1=1.5.

References

[1] *Cosmology: The Study of the Universe*. Dec. 2012. URL: https://map.gsfc.nasa.gov/universe/.

[2] Scott Dodelson and Fabian Schmidt. *Modern cosmology*. 2nd ed. Retrieved from https://www.sciencedirect.com/science/ (2023). London, United Kingdom: Academic Press, 2021. ISBN: 9780128159491.

[3] Donnacha Kirk et al. "Galaxy Alignments: Observations and Impact on Cosmology". In: *Space Science Reviews* 193.1-4 (Oct. 2015), pp. 139–211. DOI: 10.1007/s11214-015-0213-4. URL: https://arxiv.org/abs/1504.05465.

[4] Matthias Bartelmann and Peter Schneider. "Weak gravitational lensing". In: *Physics Reports* 340.4-5 (Jan. 2001), pp. 291–472. DOI: 10.1016/s0370-1573(00)00082-x. URL: https://arxiv.org/abs/astro-ph/9912508.

[5] Henk Hoekstra and Bhuvnesh Jain. "Weak Gravitational Lensing and Its Cosmological Applications". In: *Annual Review of Nuclear and Particle Science* 58.1 (Nov. 2008), pp. 99–123. DOI: 10.1146/annurev.nucl.58.110707.171151. URL: https://arxiv.org/abs/0805.0139.

[6] Nora Elisa Chisari et al. "Multitracing anisotropic non-Gaussianity with galaxy shapes". In: *Physical Review D* 94.12 (Dec. 2016). DOI: 10.1103/physrevd.94.123507. URL: https://arxiv.org/abs/1607.05232.

[7] Sukhdeep Singh and Rachel Mandelbaum. "Intrinsic alignments of BOSS LOWZ galaxies – II. Impact of shape measurement methods". In: *Monthly Notices of the Royal Astronomical Society* 457.3 (Feb. 2016), pp. 2301–2317. DOI: 10.1093/mnras/stw144. URL: https://arxiv.org/abs/1510.06752.

[8] C Danielle Leonard and Rachel Mandelbaum and. "Measuring the scale dependence of intrinsic alignments using multiple shear estimates". In: *Monthly Notices of the Royal Astronomical Society* 479.1 (June 2018), pp. 1412–1426. DOI: 10.1093/mnras/sty1444. URL: https://arxiv.org/abs/1802.08263.

[9] Cristó bal Sifón et al. "Constraints on the alignment of galaxies in galaxy clusters from ˜14 000 spectroscopic members". In: *Astronomy &amp Astrophysics* 575 (Feb. 2015), A48. DOI: 10.1051/0004-6361/201424435. URL: https://arxiv.org/abs/1406.5196.

[10] Jelte T. A. de Jong et al. "The third data release of the Kilo-Degree Survey and associated data products". In: *Astronomy &amp Astrophysics* 604 (Aug. 2017), A134. DOI: 10.1051/0004-6361/201730747. URL: https://arxiv.org/abs/1703.02991.

[11] LSST Science Collaboration et al. *LSST Science Book, Version 2.0*. 2009. arXiv: 0912.0201 [astro-ph.IM].

[12] Albert Einstein. "Kosmologische Betrachtungen zur allgemeinen Relativitätstheorie." In: *Sitzung der physikalisch-mathematischen Klasse* (Feb. 1917), pp. 142–152. URL: https://articles.adsabs.harvard.edu/pdf/1917SPAW.....142E.

[13] A. Friedmann. "Über die Krümmung des Raumes". In: *Zeitschrift fur Physik* 10 (Jan. 1922), pp. 377–386. DOI: 10.1007/BF01332580.

[14] G. Hinshaw et al. "NINE-YEAR iWILKINSON MICROWAVE ANISOTROPY PROBE/i (iWMAP/i) OBSERVATIONS: COSMOLOGICAL PARAMETER RESULTS". In: *The Astrophysical Journal Supplement Series* 208.2 (Sept. 2013), p. 19. DOI: 10.1088/0067-0049/208/2/19. URL: https://doi.org/10.1088%2F0067-0049%2F208%2F2%2F19.

[15] Adam G. Riess et al. "Cosmic Distances Calibrated to 1% Precision with Gaia EDR3 Parallaxes and Hubble Space Telescope Photometry of 75 Milky Way Cepheids Confirm Tension with {*upLambda*". In: *The Astrophysical Journal Letters* 908.1 (Feb. 2021), p. L6. DOI: 10.3847/2041-8213/abdbaf. URL: https://doi.org/10.3847%2F2041-8213%2Fabdbaf.

[16] T. M. C. Abbott et al. "Dark Energy Survey Year 3 results: Cosmological constraints from galaxy clustering and weak lensing". In: *Physical Review D* 105.2 (Jan. 2022). DOI: 10.1103/physrevd.105.023520. URL: https://doi.org/10.1103%2Fphysrevd.105.023520.

[17] and N. Aghanim et al. "iPlanck/i2018 results". In: *Astronomy &amp Astrophysics* 641 (Sept. 2020), A6. DOI: 10.1051/0004-6361/201833910. URL: https://doi.org/10.1051%2F0004-6361%2F201833910.

[18] Sarah Bridle and Lindsay King. "Dark energy constraints from cosmic shear power spectra: impact of intrinsic alignments on photometric redshift requirements". In: *New Journal of Physics* 9.12 (Dec. 2007), pp. 444–444. DOI: 10.1088/1367-2630/9/12/444. URL: https://arxiv.org/abs/0705.0166.

[19] Rachel Mandelbaum et al. "The WiggleZ Dark Energy Survey: direct constraints on blue galaxy intrinsic alignments at intermediate redshifts". In: *Monthly Notices of the Royal Astronomical Society* 410.2 (Oct. 2010), pp. 844–859. DOI: 10.1111/j.1365-2966.2010.17485.x. URL: https://arxiv.org/abs/0911.5347.pdf.

[20] Harry Johnston et al. "KiDSGAMA: Intrinsic alignment model constraints for current and future weak lensing cosmology". In: *Astronomy &amp Astrophysics* 624 (Apr. 2019), A30. DOI: 10.1051/0004-6361/201834714. URL: https://arxiv.org/abs/1811.09598.

[21] Christopher M. Hirata et al. "Intrinsic galaxy alignments from the 2SLAQ and SDSS surveys: luminosity and redshift scalings and implications for weak lensing surveys". In: *Monthly Notices of the Royal Astronomical Society* 381.3 (Oct. 2007), pp. 1197–1218. ISSN: 0035-8711. DOI: 10.1111/j.1365-2966.2007.12312.x. eprint: https://academic.oup.com/mnras/article-pdf/381/3/1197/3660046/mnras0381-1197.pdf. URL: https://doi.org/10.1111/j.1365-2966.2007.12312.x.

[22] Christopher M. Hirata and Uro š Seljak. "Intrinsic alignment-lensing interference as a contaminant of cosmic shear". In: *Phys. Rev. D* 70 (6 Sept. 2004), p. 063526. DOI: 10.1103/PhysRevD.70.063526. URL: https://link.aps.org/doi/10.1103/PhysRevD.70.063526.

[23] B. Joachimi and S. L. Bridle. "Simultaneous measurement of cosmology and intrinsic alignments using joint cosmic shear and galaxy number density correlations". In: *Astronomy &amp Astrophysics* 523 (Nov. 2010), A1. DOI: 10.1051/0004-6361/200913657. URL: https://arxiv.org/abs/0911.2454.

[24] I K Baldry et al. "Galaxy And Mass Assembly: the G02 field, Herschel–ATLAS target selection and data release 3". In: *Monthly Notices of the Royal Astronomical Society* 474.3 (Nov. 2017), pp. 3875–3888. ISSN: 0035-8711. DOI: 10.1093/mnras/stx3042. eprint: https://academic.oup.com/mnras/article-pdf/474/3/3875/23002665/stx3042.pdf. URL: https://doi.org/10.1093/mnras/stx3042.

[25] J. Liske et al. "Galaxy And Mass Assembly (GAMA): end of survey report and data release 2". In: *Monthly Notices of the Royal Astronomical Society* 452.2 (July 2015), pp. 2087–2126. ISSN: 0035-8711. DOI: 10.1093/mnras/stv1436. eprint: https://academic.oup.com/mnras/article-pdf/452/2/2087/18508439/stv1436.pdf. URL: https://doi.org/10.1093/mnras/stv1436.

[26] Jelte T. A. de Jong et al. "The first and second data releases of the Kilo-Degree Survey". In: *Astronomy &amp Astrophysics* 582 (Oct. 2015), A62. DOI: 10.1051/0004-6361/201526601. URL: https://arxiv.org/abs/1507.00742.

[27] K. Kuijken et al. "The fourth data release of the Kilo-Degree Survey: iugri/i imaging and nine-band optical-IR photometry over 1000 square degrees". In: *Astronomy &amp Astrophysics* 625 (Apr. 2019), A2. DOI: 10.1051/0004-6361/201834918. URL: https://arxiv.org/abs/1902.11265.

[28] Christos Georgiou et al. "GAMAKiDS: Alignment of galaxies in galaxy groups and its dependence on galaxy scale". In: *Astronomy &amp Astrophysics* 628 (July 2019), A31. DOI: 10.1051/0004-6361/201935810. URL: https://arxiv.org/abs/1905.00370.

[29] Christos Georgiou et al. "The dependence of intrinsic alignment of galaxies on wavelength using KiDS and GAMA". In: *Astronomy &amp Astrophysics* 622 (Feb. 2019), A90. DOI: 10.1051/0004-6361/201834219. URL: https://doi.org/10.1051%2F0004-6361%2F201834219.

[30] P. Melchior et al. "Weak gravitational lensing with deimos". In: *Monthly Notices of the Royal Astronomical Society* 412.3 (Apr. 2011), pp. 1552–1558. ISSN: 0035-8711. DOI: 10.1111/j.1365-2966.2010.17875.x. eprint: https://academic.oup.com/mnras/article-pdf/412/3/1552/3579526/mnras0412-1552.pdf. URL: https://doi.org/10.1111/j.1365-2966.2010.17875.x.

[31] E. Bertin and S. Arnouts. "SExtractor: Software for source extraction." In: 117 (June 1996), pp. 393–404. DOI: 10.1051/aas:1996164.

[32] D. J. Farrow et al. "Galaxy and mass assembly (GAMA): projected galaxy clustering". In: *Monthly Notices of the Royal Astronomical Society* 454.2 (Oct. 2015), pp. 2120–2145. DOI: 10.1093/mnras/stv2075. URL: https://doi.org/10.1093%2Fmnras%2Fstv2075.

[33] Shaun Cole. "Maximum likelihood random galaxy catalogues and luminosity function estimation". In: *Monthly Notices of the Royal Astronomical Society* (June 2011), no–no. DOI: 10.1111/j.1365-2966.2011.19093.x. URL: https://doi.org/10.1111%2Fj.1365-2966.2011.19093.x.

[34] Benjamin Joachimi et al. "Galaxy Alignments: An Overview". In: *Space Science Reviews* 193.1-4 (July 2015), pp. 1–65. DOI: 10.1007/s11214-015-0177-4. URL: https://doi.org/10.1007%2Fs11214-015-0177-4.

[35] Sukhdeep Singh, Rachel Mandelbaum, and Surhud More. "Intrinsic alignments of SDSS-III BOSS LOWZ sample galaxies". In: *Monthly Notices of the Royal Astronomical Society* 450.2 (May 2015), pp. 2195–2216. DOI: 10.1093/mnras/stv778. URL: https://doi.org/10.1093%2Fmnras%2Fstv778.

[36] Sukhdeep Singh et al. "Galaxy–galaxy lensing estimators and their covariance properties". In: *Monthly Notices of the Royal Astronomical Society* 471.4 (July 2017), pp. 3827–3844. ISSN: 0035-8711. DOI: 10.1093/mnras/stx1828. eprint: https://academic.oup.com/mnras/article-pdf/471/4/3827/19536722/stx1828.pdf. URL: https://doi.org/10.1093/mnras/stx1828.

[37] R. Mandelbaum et al. "Detection of large-scale intrinsic ellipticity–density correlation from the Sloan Digital Sky Survey and implications for weak lensing surveys". In: *Monthly Notices of the Royal Astronomical Society* 367.2 (Apr. 2006), pp. 611–626. DOI: 10.1111/j.1365-2966.2005.09946.x. URL: https://doi.org/10.1111%2Fj.1365-2966.2005.09946.x.

[38] Stephen D. Landy and Alexander S. Szalay. "Bias and Variance of Angular Correlation Functions". In: 412 (July 1993), p. 64. DOI: 10.1086/172900.

[39] Mike Jarvis. *TreeCorr: Two-point correlation functions*. Astrophysics Source Code Library, record ascl:1508.007. Aug. 2015. ascl: 1508.007.

[40] N. Chisari et al. "Redshift and luminosity evolution of the intrinsic alignments of galaxies in Horizon-AGN". In: *Monthly Notices of the Royal Astronomical Society* 461.3 (June 2016), pp. 2702–2721. DOI: 10.1093/mnras/stw1409. URL: https://doi.org/10.1093%2Fmnras%2Fstw1409.

[41] Catherine Heymans et al. "KiDS-1000 Cosmology: Multi-probe weak gravitational lensing and spectroscopic galaxy clustering constraints". In: *Astronomy &amp Astrophysics* 646 (Feb. 2021), A140. DOI: 10.1051/0004-6361/202039063. URL: https://doi.org/10.1051%2F0004-6361%2F202039063.

[42] C. Chang et al. "The effective number density of galaxies for weak lensing measurements in the LSST project". In: *Monthly Notices of the Royal Astronomical Society* 434.3 (July 2013), pp. 2121–2135. DOI: 10.1093/mnras/stt1156. URL: https://doi.org/10.1093%2Fmnras%2Fstt1156.

[43] and A. Blanchard et al. "iEuclid/i preparation". In: *Astronomy &amp Astrophysics* 642 (Oct. 2020), A191. DOI: 10.1051/0004-6361/202038071. URL: https://doi.org/10.1051%2F0004-6361%2F202038071.

[44] Antony Lewis, Anthony Challinor, and Anthony Lasenby. "Efficient computation of CMB anisotropies in closed FRW models". In: 538 (2000), pp. 473–476. DOI: 10.1086/309179. arXiv: astro-ph/9911177 [astro-ph].

[45] Naren Bhandari et al. *Fisher Matrix Stability*. 2021. arXiv: 2101.00298 [astro-ph.CO].

[46] Donnacha Kirk et al. "Optimizing spectroscopic and photometric galaxy surveys: same-sky benefits for dark energy and modified gravity". In: *Monthly Notices of the Royal Astronomical Society* 451.4 (June 2015), pp. 4424–4444. ISSN: 0035-8711. DOI: 10.1093/mnras/stv1268. eprint: https://academic.oup.com/mnras/article-pdf/451/4/4424/3903091/stv1268.pdf. URL: https://doi.org/10.1093/mnras/stv1268.

[47] Max Tegmark, Andy N. Taylor, and Alan F. Heavens. "Karhunen-Loeve Eigenvalue Problems in Cosmology: How Should We Tackle Large Data Sets?" In: *The Astrophysical Journal* 480.1 (May 1997), pp. 22–35. DOI: 10.1086/303939. URL: https://arxiv.org/abs/astro-ph/9603021.

[48] Bengt Fornberg. "Generation of Finite Difference Formulas on Arbitrarily Spaced Grids". In: *Mathematics of Computation* 51.184 (1988), pp. 699–706. ISSN: 00255718, 10886842. URL: http://www.jstor.org/stable/2008770 (visited on 06/22/2023).

[49] Dan Coe. *Fisher Matrices and Confidence Ellipses: A Quick-Start Guide and Software*. 2009. arXiv: 0906.4123 [astro-ph.IM].

[50] Andreas Albrecht et al. *Report of the Dark Energy Task Force*. 2006. arXiv: astro-ph/0609591 [astro-ph].